applied sciences

MDPI

Review

Integration of Plasmonic Structures in Photonic Waveguides Enables Novel Electromagnetic Functionalities in Photonic Circuits

Giovanni Magno [1,*], Vy Yam [2] and Béatrice Dagens [2,*]

[1] Department of Electrical and Information Engineering (DEI), Polytechnic University of Bari, 70126 Bari, Italy
[2] Centre de Nanosciences et de Nanotechnologies, CNRS, Université Paris-Saclay, 91120 Palaiseau, France; vy.yam@universite-paris-saclay.fr
* Correspondence: giovanni.magno@poliba.it (G.M.); beatrice.dagens@universite-paris-saclay.fr (B.D.)

Abstract: The development of integrated, compact, and multifunctional photonic circuits is crucial in increasing the capacity of all-optical signal processing for communications, data management, and microsystems. Plasmonics brings compactness to numerous photonic functions, but its integration into circuits is not straightforward due to insertion losses and poor mode matching. The purpose of this article is to detail the integration strategies of plasmonic structures on dielectric waveguides, and to show through some examples the variety and the application prospect of integrated plasmonic functions.

Keywords: plasmonics; photonic integrated circuits; surface plasmon; nanotweezers; couplers; strong coupling; magneto-plasmonics; nanoantennas

check for updates

Citation: Magno, G.; Yam, V.; Dagens, B. Integration of Plasmonic Structures in Photonic Waveguides Enables Novel Electromagnetic Functionalities in Photonic Circuits. *Appl. Sci.* **2023**, *13*, 12551. https://doi.org/10.3390/app132312551

Academic Editor: Andrei Lavrinenko

Received: 11 October 2023
Revised: 15 November 2023
Accepted: 17 November 2023
Published: 21 November 2023

1. Introduction

The use of optical signals for the implementation of complex computing, information processing, or communication networks is nowadays essential to meet the growing demand for data exchange. The key features of the all-optical solution include the ability to parallelize optical carriers through spectral multiplexing and specific information encodings. Photonic integrated circuits (PICs) [1–3] have been developed to generate complete optical systems and to simplify the use of different optical functions from source to modulation and signal detection. Leveraging manufacturing techniques inspired by microelectronics, planar waveguide circuits have achieved two complementary objectives: (1) to control the propagation of the optical signal in a 2D system with very low losses and (2) to facilitate the serial or parallel association of several functions without the use of spatial optical elements. Guided planar optics enables the compact integration of optical elements whose lateral dimension is on the order of the wavelength in the material. However, this dimension remains diffraction limited and cannot be further reduced.

Plasmonics has been a heavily researched field since the 2000s due to its unique capability to concentrate light on a sub-wavelength scale [4]. This entails confining light in the form of surface plasmon polaritons (SPPs); these resonant quasiparticles arise from the strong coupling between an electromagnetic wave and an electrical polarization wave carried by the surface conduction electrons of specific metals. Copper, gold, silver, and aluminum exhibit plasmonic responses, with resonance frequencies ranging from near-infrared (IR) to near-ultraviolet (UV). The electromagnetic wave that is "hooked" to the surface of the metal by plasmonic interactions has an evanescent wave profile on either side of the interface and contains a very high optical power density. Light is slowed down and concentrated at the subwavelength scale on the metal surface, facilitating enhanced interactions with any entity or material on or near the surface. Plasmons can exist in two primary forms: "propagative" on the surface of a metal film and "localized" within metal

nanostructures [5–7]. These plasmonic states exhibit several unique properties, resulting from their specific spatial profile and resonance [8]. The integration of plasmonics into photonic circuits holds significant promise for addressing several major issues and challenges in photonics and its related fields. The ability to manipulate light propagation at the subwavelength scale is undeniably of vital importance for future integrated photonic circuits. Plasmonics can facilitate the miniaturization of optical functions [9–11], enhance non-linear optical interactions [12,13], display a strong spectral and polarization dependence [14], and enable localized heating [15,16] and control of the thermally activated phase change materials [17,18], resulting in a high sensitivity of their resonance to the environment [19]. For instance, by leveraging plasmonic elements, it is possible to strongly reduce the coupling length between waveguides [20] or the position of self-images in hybrid photonic-plasmonic multi-mode interferometers (MMIs) [21], thus reducing the overall footprint of PICs.

Finally, the technological manufacture of plasmonic films and structures is compatible with low-cost processes, requiring a reduced number of steps and demonstrating improved tolerance. For all these reasons, plasmonics is expected to lead to the densification of circuits, miniaturization of normal integrated optical functions, and incorporation of novel capabilities. Furthermore, plasmonic components which are expected to be ultrafast and ultrasmall [22,23] in the future, can be integrated with photonic circuits to perform on-chip signal processing tasks. These encompass essential functions such as mode conversion [24–26], focusing [27,28], modulation [29–37], filtering [38–41], and switching [32,42–45], which are essential for the development of faster and more efficient optical communication and data processing systems. In addition, plasmonic materials and structures can be used to create extremely compact light sources [46], including plasmon lasers [47–49] and nanoscale light emitters [50–52]. Plasmonics can enhance the capabilities of purely dielectric platforms thanks to their broadband emitter (with a shorter lifetime) helping in the design of integrated coherent sources of single photons [53] for quantum applications [54–57].

However, two types of constraints limit the utilization of plasmons in optical functions: (1) the high optical losses induced by the interaction of the wave with the metal allow the use of plasmons only sparingly and (2) the excitation of plasmons from electromagnetic waves demands complex strategies, primarily due to their propagation constants, which are intrinsically higher, or even significantly higher, than those of electromagnetic waves in the surrounding environment. These two limitations can be simultaneously addressed through a smart integration of photonic circuits and plasmonic structures. In this case, embedding plasmonic structures on waveguides and photonic circuits [58] allows us to benefit from the advantages of both components, namely the low losses of dielectric waveguides and compactness of plasmons. In other words, such an integration allows us to insert plasmonic structures only where needed, and connecting them with other functions of the circuit thanks to low loss dielectric waveguides. Nevertheless, this integration poses a significant challenge due to the substantial differences in spatial extension between dielectric and plasmonic modes, which are accompanied by contrasting propagation constants. In this context, the purpose of this article is twofold. On the one hand, it reviews strategies for integrating plasmonic structures, which support localized or propagative plasmons, on dielectric waveguides. On the other hand, it demonstrates the diversity of potential applications where the synergistic integration of plasmonic features can lead to innovations.

2. Integration and Excitation of Plasmonic Structures

The incorporation of plasmonics into photonic circuits poses a significant challenge due to the contrasting spatial characteristics of plasmonic and dielectric modes. The primary hurdle lies in achieving optimal optical integration and impedance matching between metallic structures and dielectric waveguides. This integration typically necessitates a mode coupling region, the length of which depends on the specific interfacing mechanism. To assess the quality of the interfacing, the relevant indicator is the coupling efficiency,

which is defined by the ratio between the power available in the waveguide at the exit of the transfer zone and that in the dielectric guide before the transfer zone. By this definition, the coupling efficiency encompasses all types of losses generated in the coupling region, including ohmic losses and those related to mode mismatch. In this section, we will delve into the challenges related to interfacing strategies for both propagative and localized plasmon families.

2.1. Propagative Surface Plasmon

Propagative surface plasmon is generated at the interface between a metal and a dielectric material. It can propagate at several wavelengths' distance along this interface. It has the characteristic profile of a transverse magnetic (TM) wave, featuring its primary electric field component perpendicular to the interface and a secondary, smaller component in the propagation direction. Its profile also exhibits an exponential decrease, forming an evanescent profile on each interface side, as shown in Figure 1a,b.

Propagative SPP is analytically described by its dispersion curve, which is established by solving the Maxwell equations in the case of the double exponential profile [6]:

$$k_{sp}(\omega) = \frac{\omega}{c} n_{eff} = \frac{\omega}{c} \sqrt{\frac{\varepsilon_{ext}.\varepsilon_m}{\varepsilon_{ext} + \varepsilon_m}} \quad (1)$$

where k_{sp} is the wavevector of the SPP, n_{eff} represents the effective refractive index of the mode, and ε_{ext} and ε_m are the permittivity of the dielectric and the metal materials, respectively. Dispersion curves and dispersion diagrams will be extensively used in this manuscript as a powerful tool to identify the behavior of plasmonics and hybridized plasmonic–photonic modes. This tool helps to identify and engineer various coupling mechanisms. A dispersion diagram shows the relationship between the frequency f (or angular frequency $\omega = 2\pi f$) and the wavevector $k = (\omega/c) \times n_{eff}$ of a specific mode within a given observation range. It is important to note that dispersion curves for non-guided waves propagating through homogeneous media exhibit a straight-line shape that passes through the origin of the axes. The slope of these curves indicates the refractive index of the medium. An interaction between two modes with compatible polarization is expected near the crossing point of the corresponding two non-interacting dispersion curves. The result of the interaction will be the formation of two supermodes whose dispersion curves will manifest a gap (anticrossing) in the vicinity of the aforementioned crossing point. The width of the gap formed is representative of the "strength" of the interaction between the two original modes. For more details on reading and using band diagrams, see [59]. In Figure 2, the SPP dispersion curve is represented in the case of air–gold and InP–gold plasmonic modes, where gold permittivity spectrum is approximated by the Drude model [60,61] and ω_p represents the plasma resonance angular frequency in the metal. These curves reveal the primary properties of SPPs: (1) the SPP dispersion curve consistently remains below the light line of the surrounding dielectric medium, indicating that SPPs propagate with a higher wavevector (or equivalently a higher effective index) than the electromagnetic wave in this medium; (2) as the SPP frequency approaches the plasmonic resonance, i.e., $f_{sp} = \omega_{sp}/2\pi$, the dispersion curve becomes quasi-horizontal. This indicates that SPPs propagate very slowly, with a near-zero group velocity, and becomes highly confined near the metal (featuring a high k). (3) The plasmonic resonance frequency exhibits a strong dependence on the refractive index of the surrounding medium.

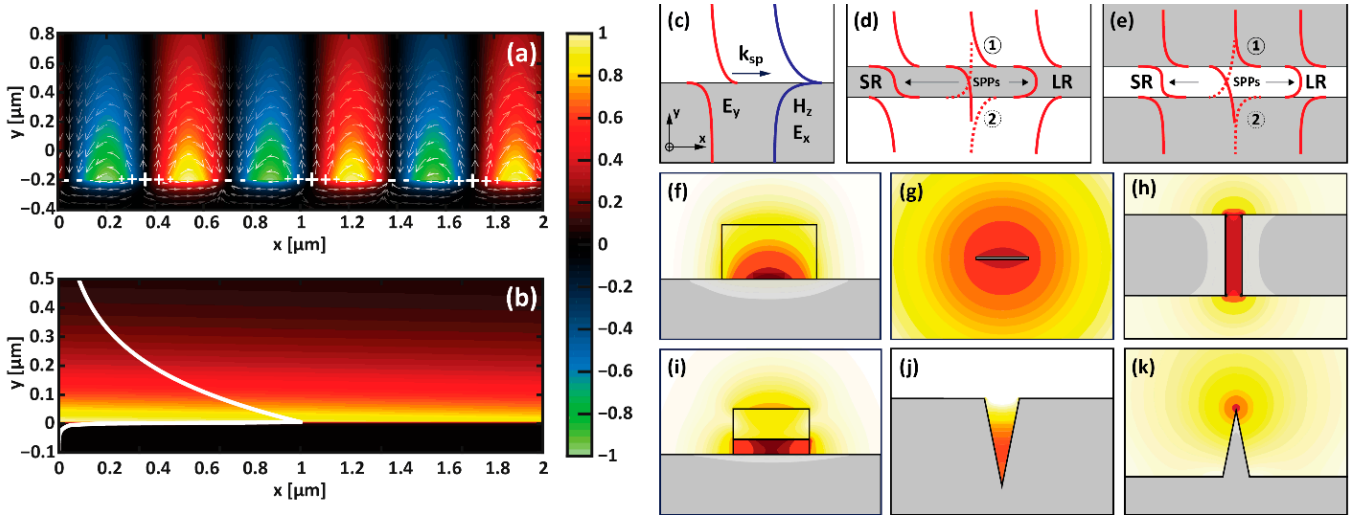

Figure 1. (**a**,**b**) Profile of a surface plasmon polariton (SPP) on an air–Au interface: (**a**) The color scale corresponds to the normalized real part of the x-component of the electric field. More specifically, the white arrows indicate the orientation of the total E field, while the + and − markers indicate the distribution of free charges on the Au surface. (**b**) The color gradient indicates the total electric field intensity. The superposed white line depicts the distribution of the intensity of the electric field x-component. (**c**–**k**) Plasmonic modes calculated for different waveguide geometries: (**c**–**e**) real part (red) of the electric field y-component when the propagation occurs along the x-direction (in-plane with respect to the figure plane). The label LR (SR) indicates the symmetric (asymmetric) coupling of two surface plasmons (SPPs) generating a "long-range" ("short-range") mode. In (**d**) and (**e**) circled numbers 1 and 2 highlight the SPPs of the individual interfaces of the respective waveguides. (**f**–**k**) Electric field intensity of the wave in the case that propagation occurs along the z-direction (out-of-plane with respect to the figure plane). Structures inspired by [62].

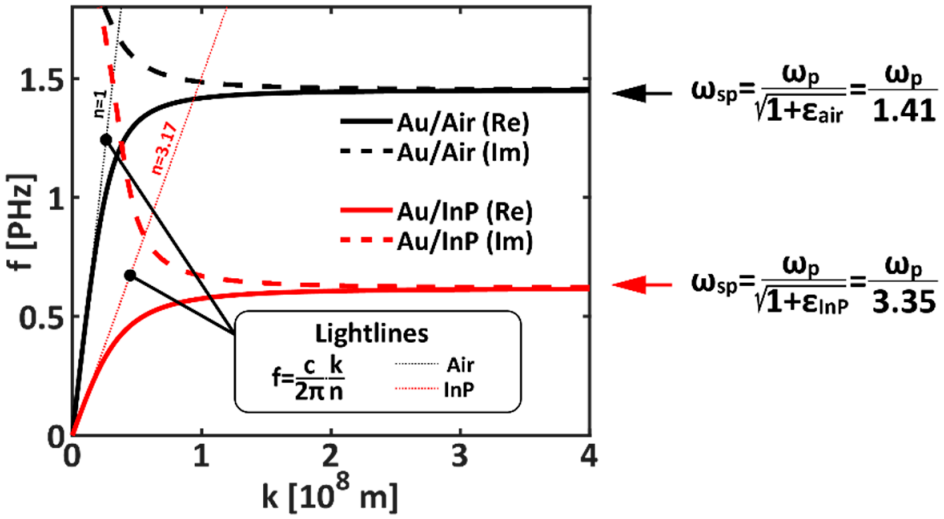

Figure 2. Dispersion curves of propagative surface plasmons at the gold–air interface and gold–InP interface. The solid (dashed) lines represent the contribution solely from the real (imaginary) part of the complex permittivity.

Several types of propagative plasmonic waveguides have been proposed, as schematized in Figure 1c–k. Some of these are designed for long-range propagation (LR) by minimizing the direct interaction between the wave energy and the metal. This is achieved through coupled SPPs on each side of a thin metallic film (Figure 1d,g) or in a metallic slot waveguide (Figure 1e,h–j). The LR-SPP is the supermode with a symmetrical phase profile and reduced losses that arises from the coupling of the two SPP modes propagating on the

two side interfaces of the metallic waveguide. Associated with it is the dual supermode, the SR (short-range) SPP, which features an asymmetrical phase profile and increased losses [62].

To benefit of their high confinement and compactness while limiting the induced losses, such plasmonic waveguides can be selectively integrated into conventional single-mode dielectric photonic waveguides. The typical interfacing schemes (Figure 3) exploit either a progressive transition (such as evanescent coupling or grating coupling) or butt-joint transition between the photonic and the plasmonic waveguides. Butt-joint transition, also called end-fire transition, [63] offers poor performance because of the significant mode shape mismatch between the plasmonic and the photonic modes (Figure 3a) and will not be discussed here.

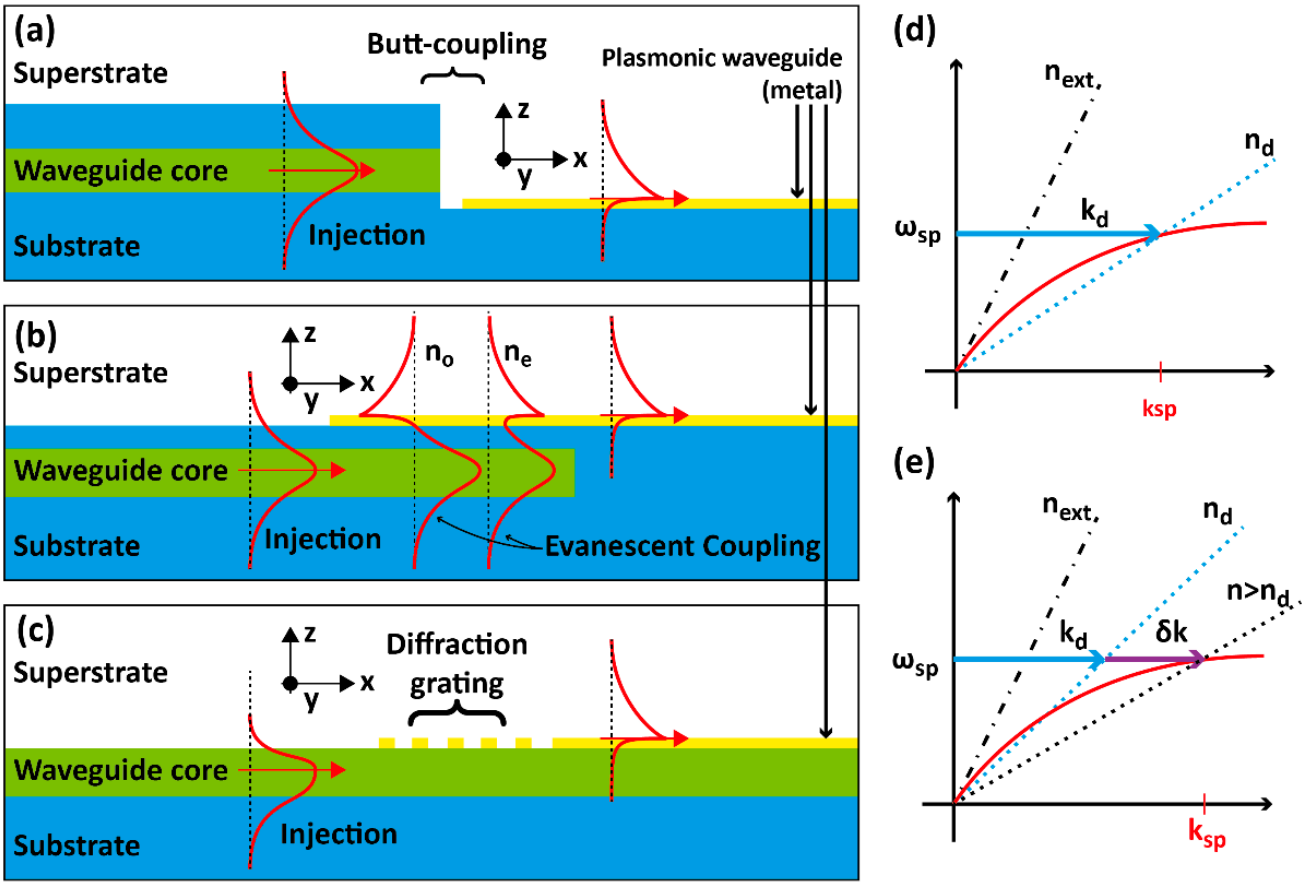

Figure 3. (**a**–**c**) Diagram illustrating three different typical ways of coupling a dielectric waveguide with a plasmonic waveguide: (**a**) end-fire coupling, (**b**) evanescent coupling, and (**c**) coupling via a diffraction grating. (**d**) The wave vector k_d of the guided mode in the dielectric waveguide is equal to that required to excite the plasmonic mode, k_{sp}. (**e**) The wave vector of the dielectric waveguide mode is not sufficient and requires an additional contribution δk, arising from the diffraction grating, to match that of the plasmonic waveguide mode.

The underlying physical mechanism harnessed through evanescent coupling (depicted in Figure 3b) or grating coupling (shown in Figure 3c) can be described by examining the dispersion curves of the involved modes (illustrated in Figure 3d,e): the dispersion curve of the SPP at the metal–dielectric interface (represented by the red curve) is situated significantly below the light line of the corresponding dielectric (characterized by an index n_{ext}). This is especially true for modes with strong plasmonic character, particularly when the SPP dispersion curve becomes quasi-horizontal. The plasmon cannot be excited by an electromagnetic wave with a propagation constant lower than k_{sp}. In the integrated configuration where the plasmonic waveguide is placed in proximity to a dielectric waveg-

uide (i.e., via a multilayer configuration as depicted in Figure 3b), the effective index n_d of the dielectric waveguide mode is higher than the refractive index of the surrounding dielectric material by construction ($n_d > n_{ext}$); this property can be used to directly excite the SPP when $k_d \cong k_{sp}$ (phase matching), since both dispersion curves cross each other (see the dispersion diagram in Figure 3d). In this case, when the polarization of the dielectric guided mode supplies the necessary z- and x- electric field components for SPP excitation, mode coupling occurs. This results in the generation of two supermodes with a hybrid photonic–plasmonic nature, featuring field symmetric and antisymmetric distributions and effective indices n_e and n_o (as shown in Figure 3b), respectively. The half-beating length of these supermodes determines the coupling length L_c of both waveguide modes, which is related to their wavevectors difference:

$$Lc = \left| \frac{1}{2} \frac{\lambda}{n_e - n_o} \right|. \quad (2)$$

After a propagation distance of L_c through the coupling region, the energy of the dielectric guided mode is totally transferred into the SPP. Such a mode coupling is called "evanescent coupling" because it involves the evanescent tails of the guided modes. The required condition ($n_d > n_{ext}$) is more easily achieved when the targeted SPP is on the opposite metallic film side with respect to the dielectric waveguide, as shown in Figure 3b. Indeed, the outside material can have a low refractive index, independent of the guided mode effective index. On the dispersion curves map, this interaction induces anticrossing of both curves. In the case of high contrast between n_{ext} and n_d, the involved plasmonic mode dispersion curve is almost flat (horizontal), and thus the generated supermodes have very different effective indices: the higher the supermode index difference, the shorter the coupling length. Thus, such a mechanism is particularly efficient when the contrast between n_{ext} and n_d is high. Delacour et al. [20] have realized this for example in the case of an SOI waveguide and a Cu plasmonic slot waveguide at 1.55 µm. The experimental coupling length equaled 0.9 µm and the coupling efficiency was estimated at 70%. In another example involving polymer waveguides, Magno et al. [64] numerically demonstrated the coupling between a SU8 on a glass waveguide and a buried plasmonic waveguide at 633 nm, with L_c = 5.3 µm and a coupling efficiency of 88%. The use of SOI waveguides is particularly interesting since, in that case, the dielectric waveguide mode has a high effective index. However, when coupling the fundamental TM mode of a high-contrast dielectric waveguide (with a high effective refractive index) to the LR-SPP mode of a thin-film plasmonic waveguide embedded in a low refractive index medium (with a low effective refractive index), it can be beneficial to employ layers of dielectric material with higher refractive indices that encapsulate the plasmonic waveguide. This helps to satisfy the phase-matching condition, as shown in [65].

If the condition $k_d \cong k_{sp}$ cannot be directly fulfilled, the guided dielectric mode must interact with a complementary structure (Figure 3c) to increase its wavevector module up to k_{sp} ($k_{sp} = k_d + \delta k$, see Figure 3e); the interaction of the dielectric waveguide mode with a periodic grating (period Λ) serves this purpose since it generates spatial harmonics whose constant propagations equal $k = k_d + p\,2\pi/\Lambda$, where p is a relative integer. The first harmonic (p = 1) is the most intense; by choosing Λ so that $k_{sp} - k_d = 2\pi/\Lambda$, the grating provides the dielectric waveguide mode with the missing component δk to excite the SPP at the dielectric/metal interface (each surface of the metal can be targeted, by proper choice of δk). In the case of a strong mismatch of the dielectric and plasmonic waveguides (i.e., if the targeted mode has a strong plasmonic character, with very high k_{sp}), successive gratings with decreasing periods can be used for a progressive adaptation, with the risk of long and lossy transitions. Tetienne et al. [66] showed in an integrated coupler made of a metallic grating for the transition between a semiconductor waveguide and a plasmonic gold film at 1.3 µm that the mode transfers along a 5.5 µm transition, with a global excitation efficiency of 24%.

2.2. Localized Surface Plasmons

Localized surface plasmons (LSPs) result from plasmonic excitation in low-dimensional metallic structures with typical dimensions lower than the wavelength in the metal. LSP modes are eigenmodes of such a subwavelength metallic structure, which behaves as a dipole or a multipole. The LSP dipolar response of the nanostructure to the electromagnetic excitation is characterized by its polarizability, which has an analytical expression in case of "simple" shapes and a homogeneous surrounding medium [67].

The excited dipole in a plasmonic nanoparticle radiates itself an electromagnetic wave of the same frequency, which can excite another plasmonic nanostructure with similar resonance; in this way, plasmonic nanostructure assembly may support collective resonances and/or propagate energy from nanostructure to the next [68]. An LSP chain dispersion curve can be thus established by using an analytical model in a homogeneous medium [69] or numerical methods in a general case. For instance, Figure 4 shows the dispersion curve, calculated using the FDTD method, of a plasmonic chain composed of gold nanocylinders with elliptical cross-sections placed on top of a semi-infinite Si substrate. The LSP chain dispersion curve displays a similar overall behavior as that of the SPP: it is positioned below the light line and exhibits a nearly horizontal slope at the highest k vectors. In other words, the collective modes of the LSP chain propagate through the chain elements as they do in a waveguide despite the intrinsic discontinuity of the metallic elements.

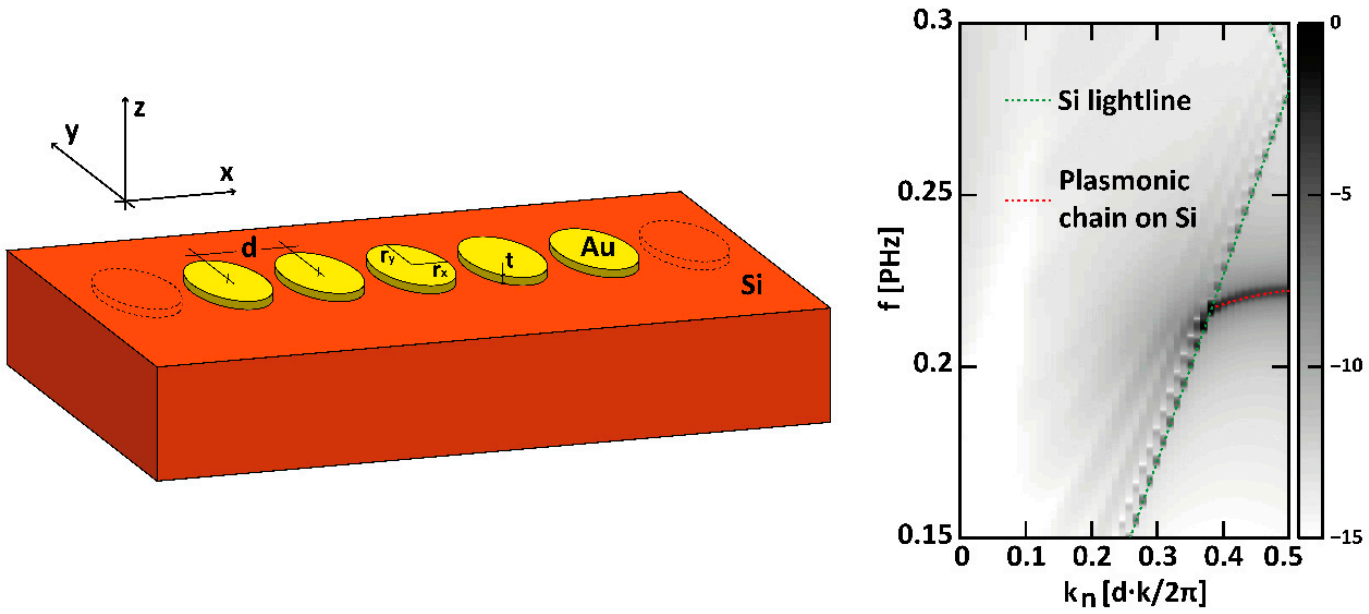

Figure 4. (**left**) Sketch of an infinite plasmonic chain of gold ellipsoidal nanocylinders placed on top of a semi-infinite Si substrate. (**right**) FDTD-calculated dispersion curve of the plasmonic transverse chain mode when d = 150 nm, r_x = 42.5 nm, r_y = 100 nm, and t = 30 nm. The red and the green dashed curves highlight the plasmonic chain mode and the Si light line, respectively.

Furthermore, chains of plasmonic nanoantennas have the ability to support topologically non-trivial modes (edge states resembling topological insulators) [70–74], bound states in the continuum [75–77], and surface lattice resonances [78–81].

LSPs in a subwavelength structure enable very high light confinement, with enhanced miniaturization and electromagnetic field concentration with respect to 2D plasmonic films. Nevertheless, the excitation of a single LSP structure is very inefficient because of the high mismatch between its resonant mode size and diffraction-limited electromagnetic waves. The excitation efficiency of such a single nanostructure deposited on a silicon nitride waveguide reaches less than 10% (9.7% in [82]). To transfer all the energy of the dielectric guided mode into an LSP, a viable solution is to exploit the waveguides' evanescent coupling as shown above, considering a plasmonic chain instead of a plasmonic

metallic film [83]. The typical structure is made of a MNP metallic nanoparticle (MNP) chain integrated on or near a dielectric waveguide (Figure 5). The chain can be designed to propagate either TE or TM modes and can be in any position near the waveguide if their relative distance allows the evanescent tail of the dielectric mode to overlap with the LSPs. In addition to enabling the LSP excitation, such a strongly coupled structure has specific properties, as described below.

2.2.1. Coupling Efficiency

Figure 5 shows the FDTD calculations of a TE mode in a dielectric waveguide evanescently coupled to an LSP chain. The (infinite) LSP chain is directly deposited on a SOI waveguide, and Figure 5b–d reveals the anticrossing of both dispersion curves which generates the resulting odd and even supermodes. The strong coupling between both waveguides, in addition to the low slope of the LSP chain curve, induces supermodes with very different indices and thus a very short coupling length. Depending on the wavelength, the fundamental TE mode of a SOI waveguide can be totally transferred in the 4th or 5th MNP of the finite chain [83], which corresponds to a ~600 nm coupling length (Figure 5f). The coupling efficiency is near 99% in the case of a 5 MNP chain (Figure 5e). Due to a lower dielectric effective index, the optimal configuration in the case of a Si_3N_4 waveguide at 633 nm enables a total transfer of the mode energy in an 8 MNP chain with a coupling length of ~800 nm.

In fact, the energy transfer efficiency is improved with respect to a single MNP case as soon as a second MNP is involved ("dimer" chain). In return, however, the chain length increase implies an increase in ohmic losses. In order to exploit the high electromagnetic power density at the surface of a nanoparticle, the best compromise must be thus identified between the efficient energy transfer induced by the collective resonance in the chain and the ohmic losses.

2.2.2. Strong Coupling

In the configuration presented in Figure 5a, the strong coupling [84] between the plasmonic and SOI waveguides induces additional distinctive characteristics specific to this system. Firstly, over a wide range of frequencies, the supermodes propagate in a vortex-like manner. These vortices are related to slow modes [85] and can be also characterized by their phase profile along the chain [86]. Secondly, due to strong coupling, supermodes can also be excited beyond the light lines of the different materials surrounding the plasmonic chain. Thus, they can be excited as radiative modes above the light line of the confinement layer (silica here) and/or below the highest index material light line (silicon here) in the non-guided mode region (see the dispersion diagrams in Figure 5b,c). As a consequence, the plasmonic mode hybridization can modify their radiative or guided nature, or even extend their possible frequency range.

Moreover, nanoantenna arrays integrated on waveguides can take advantage of tapering their dimensions within the integration plane to achieve enhanced control over coupling characteristics. For instance, tapering the period of the plasmonic array enables efficient mode conversion and excitation of higher-order modes in the waveguide [87].

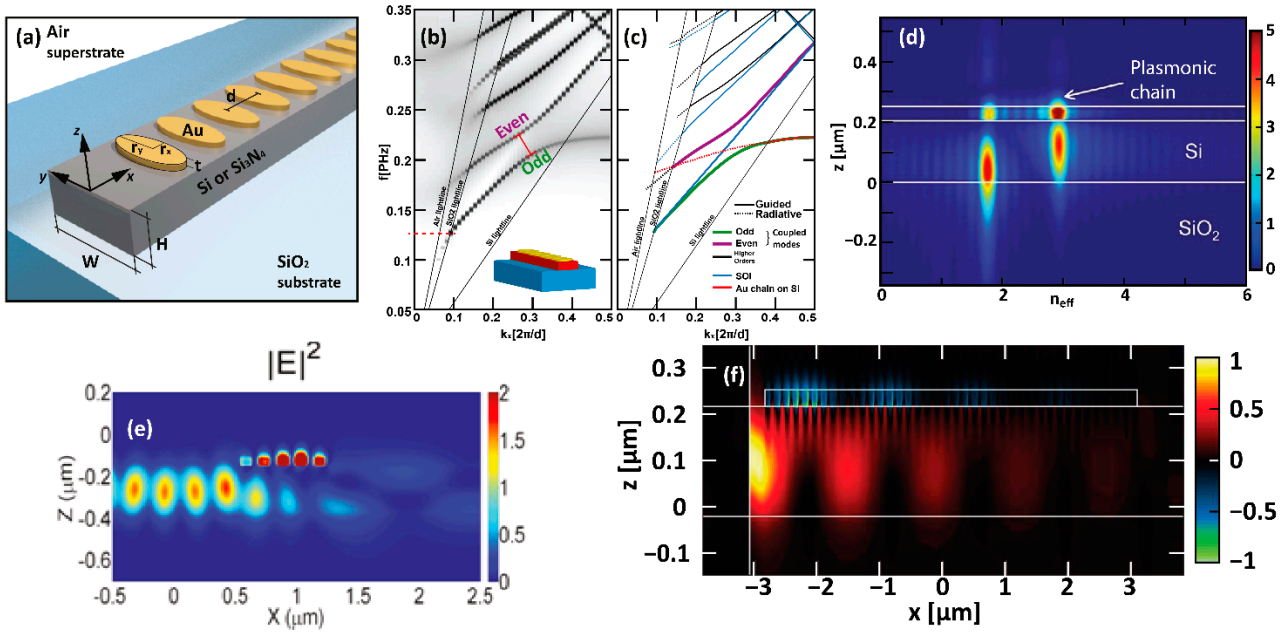

Figure 5. Localized plasmon waveguide integrated on SOI (TE mode). (**a**) Sketch of the structure. (**b**,**c**) FDTD-calculated dispersion curves for d = 150 nm, r_x = 42.5 nm, r_y = 100 nm, t = 30 nm (the permittivity of gold is obtained using a Drude model fitted to ellipsometric measurements). (**d**) A typical spatial distribution of the two supermodes. (**e**,**f**) Electric field intensity in the case of a finite chain of (**e**) 5 or (**f**) 20 nanoparticles. Inspired by [85].

3. Surface Plasmons in Photonic Integrated Circuits

Surface plasmons in PICs are expected to considerably improve some photonic functions thanks to the subwavelength light concentration and the local field enhancement they induce. Reciprocally, the use of guided photonics to excite plasmonic structures leads to very efficient light coupling in these structures. The improvement is particularly marked in the case of very compact localized plasmonic patterns. We will focus here on four examples of different uses of integrated plasmonics.

3.1. LSPR for Molecules Biosensing

Plasmonic biosensing [88–92] was initially mainly based on functionalized gold films and propagative plasmons (SPR technology) to exploit localized surface plasmons in metallic nanostructures arrays on glass (LSPR technology) [19,93], as used in present commercialized setups. Such functionalized substrates are used in complex 3D optic systems made of prisms and lenses with the following principle: metallic (gold) nanostructures are grafted with molecule receptors (often thiols), and molecules to be detected are brought to these receptors by a microfluidic system. The trapping of the molecules is detected by the plasmonic resonance shift induced by the complex index modification near the metallic structure, where a diffraction-limited laser beam in the Kretchman configuration excites the plasmon [94]. In LSPR systems, the sensor sensitivity is limited by the optical power available for each functionalized nanostructure because of the poor mode matching, as explained above. By using the same detection principle, the excitation of LSPs can be realized in guided configurations, with two main advantages:

- The excitation electromagnetic energy can be fully transferred to the LSP, like in the case of a 5 MNP chain [95], leading to an improved sensitivity,
- Parallel or series sensing areas can be implemented on the chip with the same optical source, considerably enhancing the global analysis capacity.

Figure 6 shows such a guided LSPR sensor including a chain or 5 MNPs, and the resonance spectral shift induced by grafted thiol molecules which form an equivalent layer

with a thickness of t = 2nm and index of n = 1 + Δn. This shift (Δλ) has been numerically evaluated and experimentally checked as corresponding to the relation Δλ(nm) ≈ 27 (t(nm) × Δn)$^{0.75}$. The expected sensitivity to the environment of this sensor integrated on SOI can reach a value up to 270 nm/RIU (Refractive Index Unit) [95].

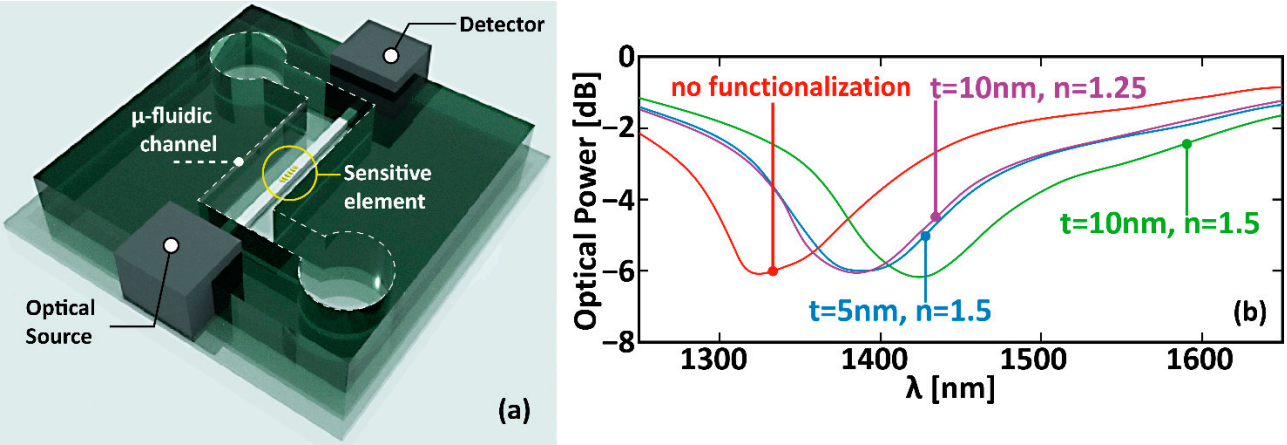

Figure 6. (**a**) Sketch of a sensor exploiting LSPRs: a chain of gold nanocylinders is integrated on top of an SOI waveguide within a microfluidic circuit. (**b**) Transmittance calculated for different equivalent thicknesses t of molecules grafted onto the metal pads [95]. Specifically, t represents the thickness of a layer having an index equal to n covering each NP. This result has been validated experimentally for t = 2 nm.

3.2. Plasmonic Nano-Tweezers and Nano-Manipulators

Tweezers and manipulators that function at the nanoscale are in very high demand for biosensing and the analysis of nano-objects. High electromagnetic density variation around plasmonic nanostructures enables optical tweezing based on the gradient force [96], which results from mechanical and optical momentum exchange between the object and the photons. The gradient force acts as an elastic trap for an object entering its influence area, with a stiffness proportional to the local optical power derivative.

3.2.1. Basis on Optical Tweezers

Optical tweezers are made of a focused optical beam, which is diffraction limited in the case of a free space beam, which generates two forces on an object (Figure 7, left): the gradient force and the pressure (or diffusion or absorption) force. The former pulls the object towards the highest optical density, usually transversally to the optical beam and up to its center; the latter pushes the object along the beam propagation axis and direction. These forces are expressed as follows:

$$\text{Gradient force}: \; \boldsymbol{F}_g = \frac{1}{4}\,\alpha_{Re}\nabla|\boldsymbol{E}|^2$$

$$\text{Pressure force}: \; \boldsymbol{F}_s = -\frac{1}{2}\,\alpha_{Im}\text{Im}\{\boldsymbol{E}.\nabla(\boldsymbol{E}^*)\}$$

where α is the object polarizability: $\alpha = \alpha_{Re} + j\alpha_{Im}$.

The gradient force is thus the trapping force. It is proportional to the optical power density (or the electric field square modulus) gradient and to the real part of the object polarizability. The trapping strength is represented by its stiffness and defined by the derivative of the exerted forces. Negative (positive) stiffness corresponds to an attractive (repulsive) force.

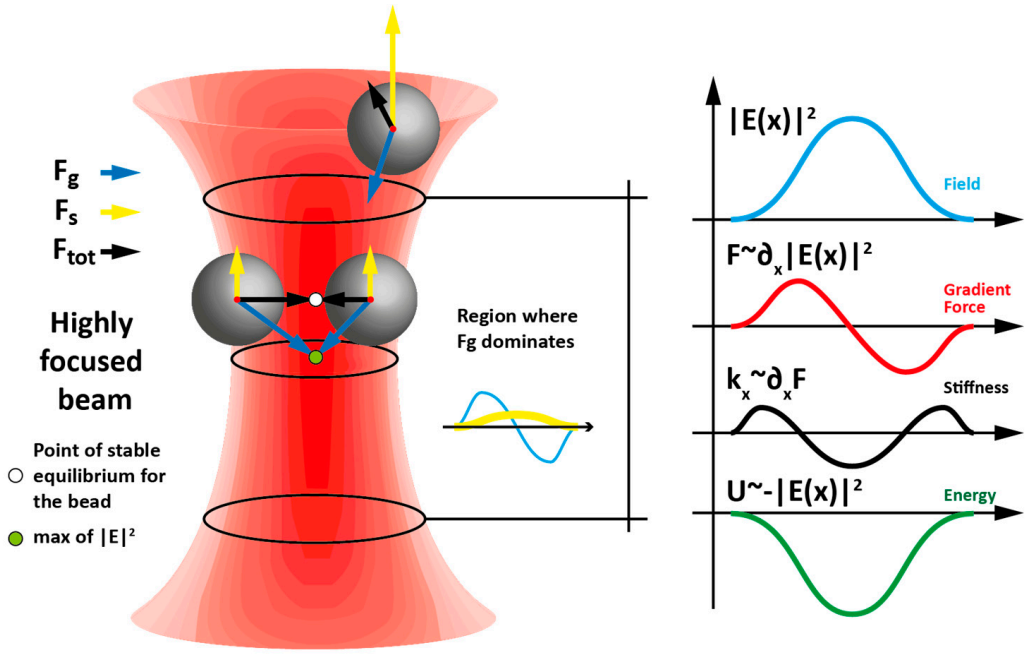

Figure 7. Sketch of optical tweezing in a Gaussian beam. The total force $\mathbf{F}_{tot}$ represents the sum of the gradient force $\mathbf{F}_g$ and scattering force $\mathbf{F}_s$.

The trap characteristics can be evaluated as follows:

- If the trapped object does not modify the local electromagnetic field, the optical density map is calculated first, and then the trap characteristics are deduced from $\boldsymbol{F_g}$ and $\boldsymbol{F_s}$ calculations for different object positions.
- If the presence of the object induces a non-negligible perturbation, the optical field must be calculated, and the Maxwell stress tensor must be fully integrated for all the possible positions of the object.

The optimal trap, in terms of temporal and spatial stability, is obtained for object sizes slightly larger than that of the optical beam (or than the optical power density high variations area) to benefit from the highest gradients. Stable trapping criteria (from Ashkin [96]) state that the potential well must be ten times higher than the thermal energy k_BT_0. The total optical power can thus be used to increase the stability as well as the stiffness of a trap.

Optical beams enable the trapping of objects around 1 µm in size with a few mW of power, compatible with biological objects whose index is around 1.3 (water). To trap smaller or less dense objects (for air or water quality analysis), more abrupt optical density gradients are required, such as those generated around plasmonic structures.

3.2.2. Plasmonic Tweezers

Plasmonic (nano-)tweezers have been extensively studied, mainly in non-integrated configurations. Integrated localized plasmonics may enable extremely high gradient forces thanks to the powerful combination of "high optical density" and "high excitation efficiency" of integrated resonant structures. Numerical and experimental demonstrations aimed at trapping polystyrene beads of different diameters in the three published examples are shown in Figure 8. In the first case (Figure 8a), the dimensions of the metal nanostructures only enable the use of propagative plasmons. The 5 µm diameter disks are positioned along a 15 µm grid on the top of a multimode waveguide; 1 µm diameter PS beads are trapped with an injected power of 20 mW, leading to a trap stiffness of -17 fN/µm. The second structure (Figure 8b) was designed to trap 20 nm diameter beads, concentrating the light in the narrow gap of the butterfly structure; the theoretically achievable force reached more than 650 pN/W in the case of a 5 nm gap. Comparable results were obtained by

varying the dimer geometry within the integration plane, as illustrated in [97]. The third example corresponds to an integrated MNP chain which maximizes the LSP excitation. In the case of a 4 MNP chain with a 150 nm period, the exerted force on a 500 nm diameter PS bead reached ~40 pN/W with a stiffness of −2408 fN/nm/W. The considered power refers to the power injected into the waveguide.

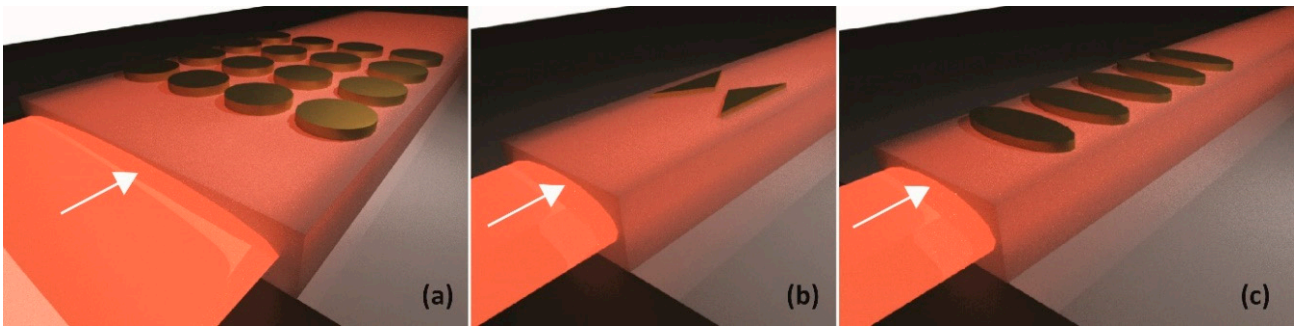

Figure 8. Plasmonic nanostructures integrated on top of a waveguide: (**a**) array of metallic pads supporting propagative resonances (SPPs) (according to [98]); (**b**) single bowtie nanoantenna (according to [96]); (**c**) chain of coupled nanocylinders (according to [99]).

In this kind of chain, the plasmonic modes generate a high spot at the ellipsoidal nanocylinder edges, separated by a distance of around 200 nm (see Figure 9a). To trap nano-objects, the trap must be compact. The gap between MNPs can be smaller to create a resonant nano-gap, like in the longitudinal dimer represented in Figure 9b. As simulated in Figure 9 (bottom, right), a gap smaller than 40 nm is required to trap a 50 nm radius PS bead with an injected power of 10 mW [99]. Experimentally, 500 nm diameter PS beads have been trapped by injecting 6 mW (at 1550 nm) into a waveguide functionalized by a 20 gold NP chain, with a measured stiffness of -5.1×10^{-1} fN·nm^{-1} in the propagation direction (x). Considering the fibered optical injection losses in the waveguide, the stiffness was estimated at -10^2 fN·nm^{-1}W^{-1}.

Chains of metallic nanostructures can be realized for any shape of resonant nanoparticles (disks, ellipsoidal cylinders, butterflies, etc.), and thus can be adapted to trap different objects, as shown in Figure 10 for a transverse dimer chain.

Moreover, the spectral and spatial dependence of the MNP chain excitation allows all-optical trapped object manipulation. Figure 11 shows the stable trapping positions (pale pink lines) versus the excitation wavelength in the case of a 4 MNP chain and 10 mW injected power [100]. In this case, the integrated nanotweezers was designed to manipulate a biological object modeled as a spherical bead with a radius of 250 nm and with a refractive index as low as 1.38. By adjusting the source wavelength to regulate the phase mismatch of the supermodes housed by the structure, it is possible to manipulate the trapped object along the plasmonic chain. Other configurations of an integrated plasmonic "conveyor belt" have been proposed, based on the MNP size diversity [101]. Such structures are also able to trap and self-assemble groups of nano-objects [102].

3.3. Plasmonic Antennas

The integration of plasmonic antennas into photonic circuits presents opportunities for mutual benefits. On the one hand, nanoantennas can take advantage of feeding schemes embedded in PICs. These schemes can be interconnected and combined with circuit elements that enable the control of the feed phase [103–106], facilitating functions such as beam shaping and steering [107]. Integrated coupling methods can also lead to highly effective excitations of the radiating elements. On the other hand, integrating plasmonic nanoantennas into PICs holds potential for short-range on-chip and chip-to-chip wireless communication [108,109]. The growing demand for high-speed data communications within data centers and high-performance computing platforms, driven by advancements

in electronic devices and multi-core architectures, has led to rapidly increasing speed requirements. To address the limitations of copper-based interconnections [110,111], such as high power consumption, heat dissipation, latency, signal losses, crosstalk, and bandwidth constraints, the development of parallel optical short-range links has been proposed and pursued [108,109,112]. Various types of antennas, such as Vivaldi-type antennas (leveraging propagative plasmons, [113–115]), Yagi–Uda antennas (acting as resonator–collectors), or LSP chain antennas, can be considered for this purpose. As previously discussed, the energy transfer between the PIC waveguide and the antenna is the key issue for functional efficiency.

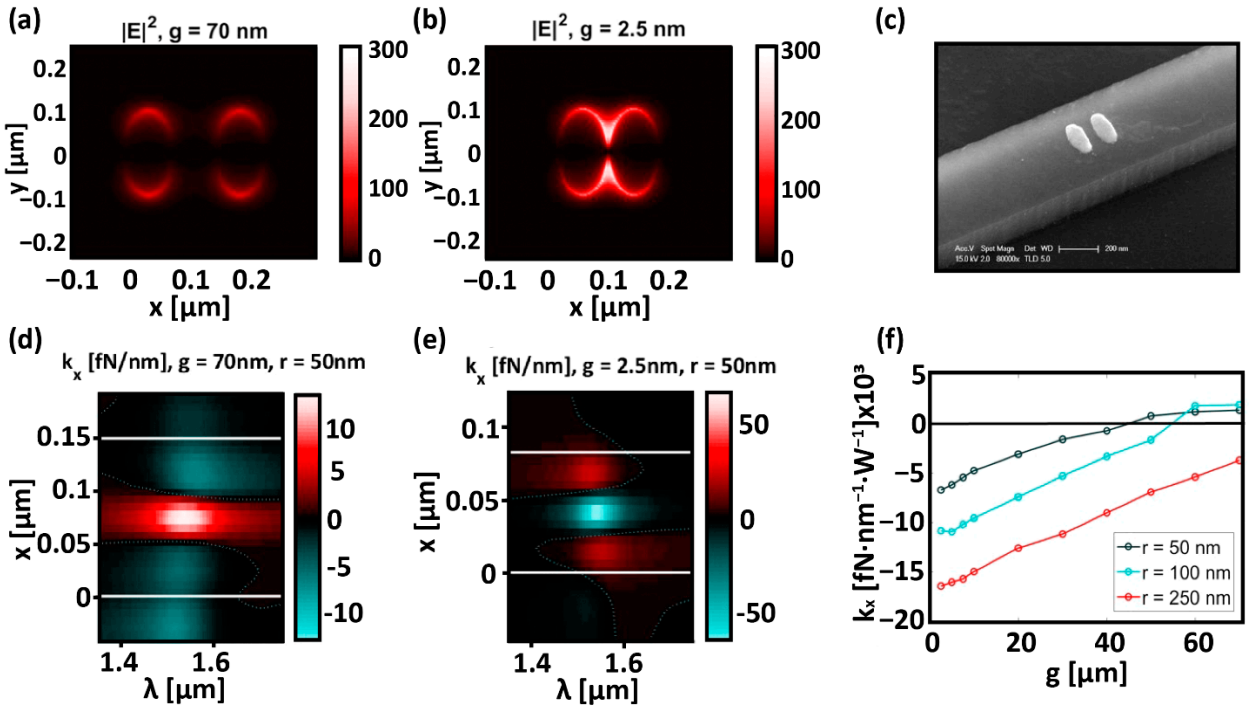

Figure 9. (**a**–**f**) Integrated longitudinal dimer chain for trapping nano-objects [99]. (**a**,**b**,**e**,**f**) FDTD simulation obtained for an injected power of 10 mW. (**a**,**b**) Squared absolute value of the electric field and (**d**,**e**) stiffness along the *x*-axis k_x calculated on the plane of the dimer top facet when the dimer gap g is equal to (**a**) 70 nm and (**b**) 2.5 nm, respectively. (**f**) Stiffness k_x as a function of the gap g calculated for different values of the radius of the bead interacting with the device. (**c**) Scanning electron microscopy image of the fabricated sample.

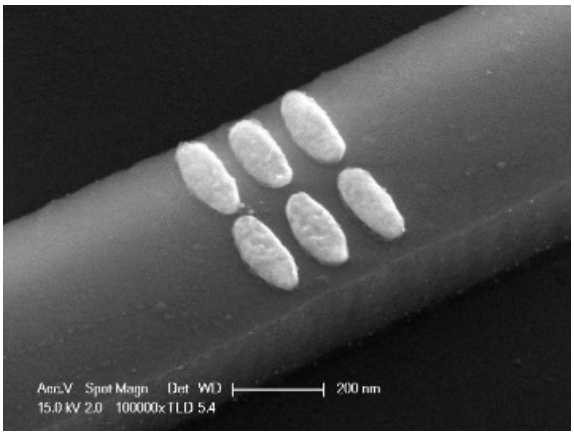

Figure 10. Scanning electron microscopy image of a 3-period dimer chain integrated on an SOI waveguide.

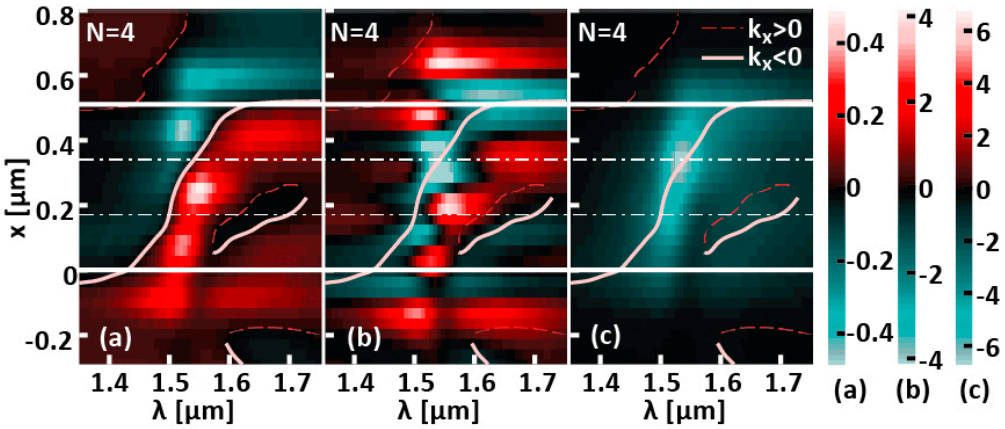

Figure 11. (**a**) Optical force (pN) and (**b**) stiffness (fN/nm) along the x-axis, as well as (**c**) optical force (pN) along the z-axis, calculated as a function of the wavelength and position of a spherical biological object. The latter is grazing along the x-axis on the top facet of a plasmonic chain composed of 4 NPs integrated on top of an SOI waveguide. The chain element spacing (center to center) is 150 nm. This device enables the trapping and displacement of the biological object along the plasmonic chain axis [100].

In all these cases, it is imperative for the plasmonic structure to exhibit radiative behavior, meaning its dispersion curve must fall within the light cone while also effectively coupling with the waveguide modes. In the case of Vivaldi antennas, these properties are obtained by progressively changing the antenna shape and the waveguide structure along the propagation axis. A progressive energy transfer is realized by evanescent coupling, and the excited plasmon radiates at the end of the suspended antenna. The integrated directivity is similar to the free space Vivaldi antenna and enables us to target the receiver, which is itself integrated, as shown in Figure 12.

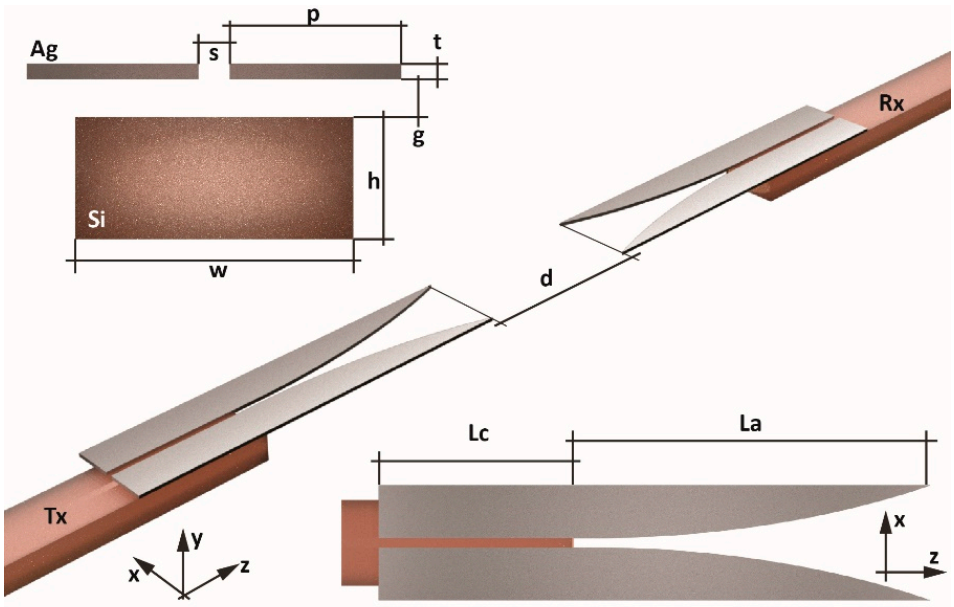

Figure 12. Vivaldi antenna integrated on an SOI waveguide as part of an on-chip optical interconnection system (inspired by [115]).

Integrated Yagi–Uda antennas are made of a resonant plasmonic "receiver", positioned between the "director" (made of several resonance-shifted resonators) and a "reflector" (wider metallic element). The radiative part of the antenna is the "receiver", whereas the other elements play roles of confinement (of the incident signal) or directivity (of the

radiated signal) in the axe of the "director" chain. When the Yagi–Uda plasmonic antenna is integrated on a substrate or a waveguide, as shown in Figure 13, the emission is slightly deviated from the axis of the antenna elements in the case of surrounding optical index asymmetry. The typical radiation diagram thus shows emission towards the higher index medium, usually the substrate. The angle depends mainly on the index difference.

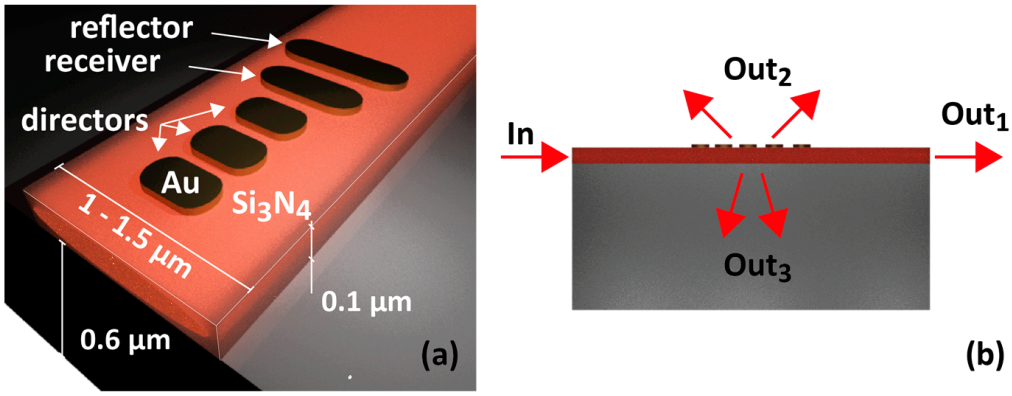

Figure 13. (**a**,**b**) Yagi–Uda antenna integrated into a waveguide. (**a**) 3D sketch of the structure. (**b**) Side view of the structure, red arrows represent the direction of light flow. The radiation is preferentially directed towards the highest optical index (substrate). Inspired by [116].

Recently, it has been demonstrated that specific engineered arrangements of elementary nanoantennas, strategically positioned on the surface of a silicon waveguide, can couple the two orthogonal polarizations of incident light into different directions and modes of the underlying waveguide, thus achieving a demultiplexing function [117].

A periodic chain made of identical MNPs can also realize controlled directivity of an "LSP" antenna, which is evanescently coupled to a dielectric waveguide. In order to obtain collective and radiative resonance, the chain is designed as a diffraction grating while keeping a sufficiently short period to enable dipole coupling along the chain [118,119]. The latter property enables efficient interfacing of the antenna with the dielectric waveguide (Figure 14). The diffraction grating controls the emission direction (period) and directivity (chain length). For symmetry reasons, as soon as the grating order is higher than 1, the light is diffracted simultaneously in two directions: toward the substrate and the superstrate. The emission angle is defined with respect to the guided propagation axis as follows: in the case of homogeneous surrounding index n_s, $\theta = arcsin\left(\frac{n_{eff}}{n_s} - \frac{m.\lambda}{d.n_s}\right)$ where d is the grating period, m is the grating order, and n_{eff} is the effective index of the guided mode. With respect to the usual dielectric or metallic gratings, this resonant chain grating offers additional degrees of freedom:

- The chain resonance modifies the coupling efficiency independently of the emission angle and directivity control; the MNP size is chosen to have a resonant or resonant-shifted chain.
- The chain can be positioned freely around the waveguide, without diffraction efficiency modification as long as the chain and waveguide mode overlap remains similar.
- The chain period determines the emission angle independently of the coupling efficiency.
- Several chains can be simultaneously excited, for example, to shape the radiation diagram: two chains on both sides of the waveguide generate radiation similar to Young's slit interferences.

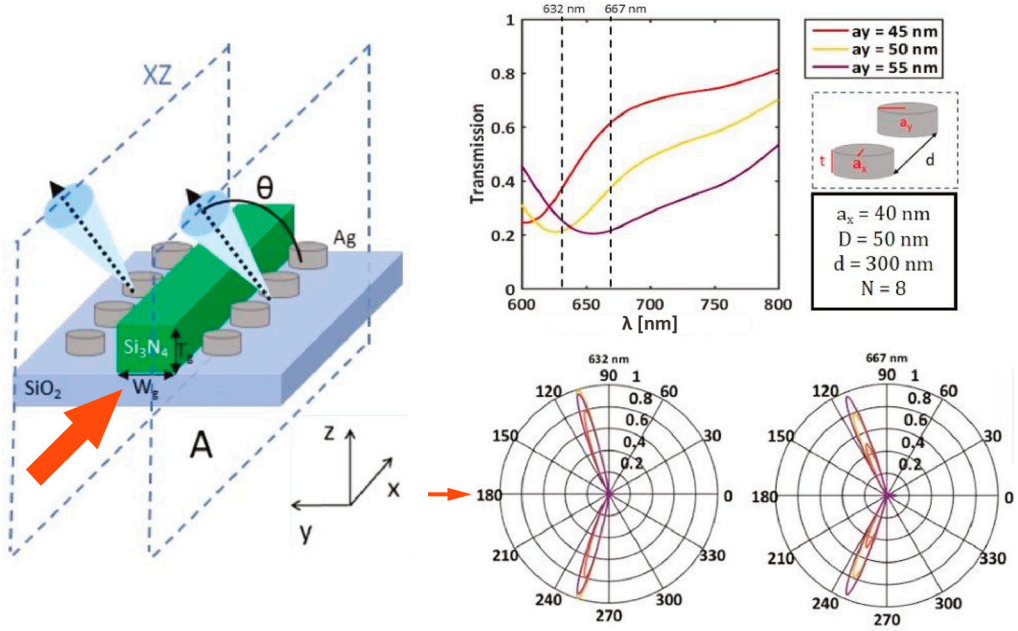

Figure 14. Array of integrated plasmonic nanoantennas dedicated to the independent control of directivity, direction, and intensity of radiation, inspired by [120]. a_x and a_y represent the radii of the ellipsoidal sections of the MNPs, t is the thickness of the MNPs, N is the number of MNPs per chain, d is the center-to-center distance, and D is the smallest distance between the MNPs and the dielectric guide. The red arrow indicates the direction of light injection.

In Figure 14, a double 8 ellipsoidal MNP chain with d = 300 nm is positioned at D = 50 nm from a silicon nitride waveguide. The minima of optical transmission through the waveguide indicate the chain resonances for three values of ellipses with a long axis radius of a_y. The radiation diagrams are calculated for two different wavelengths: they show the independence of the emission angle and the coupling efficiency (proportional to the radiative power). This control of the coupling efficiency was verified experimentally [120]. It can vary from 10 to 50% by changing only the major axis of the nanocylinders a_y, offering control of the radiated power without changing the radiation diagram.

3.4. Integrated Magneto-Plasmonics

Plasmonics is particularly relevant for enhancing perturbative physical effects such as magneto-optics (MOs) [121]. Magneto-optical effects are related to the action of the magnetization of a material on the propagation of an optical wave through it. This action is expressed by the non-diagonal elements of the permittivity tensor of the MO material, which is as follows for an otherwise isotropic material:

$$\varepsilon = \begin{pmatrix} \varepsilon_{iso} & +ig_z & -ig_y \\ -ig_z & \varepsilon_{iso} & +ig_x \\ +ig_y & -ig_x & \varepsilon_{iso} \end{pmatrix} \quad (3)$$

where g_u (u = x,y,z) are the gyrotropy constants, which are complex values in the most general case. The interaction of an electromagnetic wave with an MO material impacts its electric field through the complex coupling of its components (E_x, E_y, E_z), which can modify the wave polarization, amplitude, and/or phase. Since the permittivity tensor is antisymmetric, this interaction is non-reciprocal; it is reversed by inversion of the propagation direction or the magnetization direction. In other words, this effect induces time-symmetry breaking. Usual MO materials are either metallic (Fe, Co, Ni, and alloys) or dielectric like ferrite or garnet oxides (BIG, YIG, Ce:YIG). Combined with a plasmonic metal, these materials induce magneto-plasmonic effects, with enhanced effective complex gyrotropies. Magneto-plasmonic multilayered structures have been mainly studied in non-

guided configurations such as single nanostructures or hybrid membranes [122], arrays of nanostructures [123,124], alternating silver and garnet layers metamaterials [125], or reconfigurable metasurfaces or arrays of nanoantennas [126,127]. Magneto-optical interactions with propagative plasmons have been also studied in grating structuration [128,129].

Nevertheless, only a few (theoretical) magneto-plasmonic structures were proposed in waveguiding configurations [130,131]. The main interest in these MO or magneto-plasmonic structures is to realize integrated non-reciprocal transmission of light, like optical isolation or circulation. Such functions can considerably enrich the architecture of photonic circuits.

The non-reciprocal transmission is obtained only if all the spatial symmetries are also broken, in addition to the time-symmetry breaking. The non-reciprocity of an integrated isolator is defined as the ratio between its forward and backward transmissions, denoted as T^+ et T^-, often expressed in decibels as 10 Log(T^+ /T^-). A figure of merit (FoM) Δ can be defined to account for the trade-off between non-reciprocity and insertion losses:

$$\Delta = \begin{cases} \frac{T^+ - T^-}{T^+} & if \quad T^+ > T^- \\ \frac{T^+ - T^-}{T^-} & if \quad T^+ < T^- \end{cases} \tag{4}$$

Several MO effects have been identified, all related to the permittivity tensor and gyrotropies, but considering the different configurations of light polarization, magnetization orientations, and interaction nature (bulk or at interfaces) [132]. Among all these configurations, the most relevant for integrated guided structures is the TMOKE (transverse magneto-optical effect); indeed, TMOKE occurs at interfaces between MO and dielectric or metallic materials, it preserves light polarization and only modifies the propagation wavevector of the light. Such a configuration is easily obtained in multi-layered planar structures, and spatial symmetry breaking is also just a matter of the appropriate geometry (Figure 15).

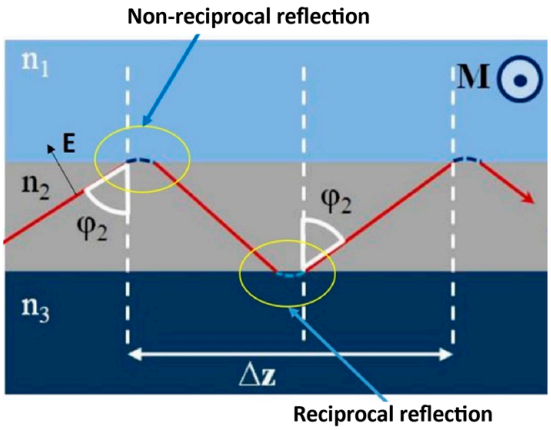

Figure 15. TMOKE (transverse magneto-optical Kerr effect) applied to a planar waveguide. The top layer (n_1) is a material with magneto-optical properties.

Many guided structures based on TMOKE have been demonstrated, which were based on an MO metallic layer deposited on a dielectric or semiconductor waveguide, interacting with the TE [133] or TM [134] mode; MO garnet transferred on a semiconductor interferometer [135] or on a ring resonator [136]; garnet interferometer including a thin silver film [131]; and gold grating on a garnet waveguide [137]. In the latter structure, the non-reciprocal effect is enhanced by plasmonic light concentration; in addition, its sign is controlled by the grating slit modes coupling with the propagative surface plasmon. In this way, non-reciprocity can be inversed by the proper grating design while keeping the magnetization direction unchanged.

Such a structure is represented in Figure 16: the gold grating is placed on the top of an MO garnet (BIG) waveguide, whose magnetization is in z direction. The guided TM mode is injected into the structure and interacts with the plasmonic top-grating and with the Fabry–Perot modes inside the grating slits. Their coupling induces anticrossing in the dispersion curves (Figure 16b) and non-reciprocity enhancement on each side of this anticrossing. Because of the resonant character of the structure, the isolation is limited to a narrow bandwidth, and the FoM reaches 40%.

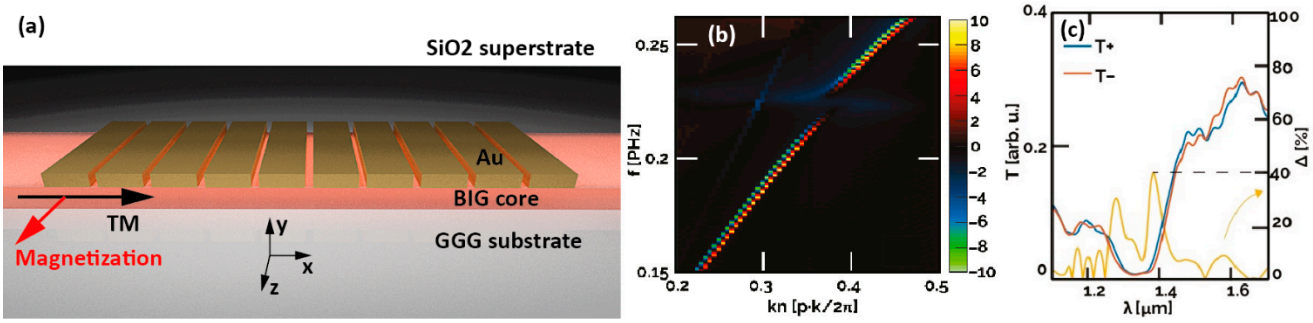

Figure 16. (**a**) Sketch of a non-reciprocal waveguide with integrated plasmonic grating on garnet. Here, the BIG layer is the magneto-optical material. (**b**) Non-reciprocal shift of the band structure and (**c**) non-reciprocal transmittances obtained by means of FDTD simulations [137].

Following the same principle, by positioning the plasmonic grating on the side of the waveguide, t**he** TE mode undergoes an isolation ratio higher than 20 dB (8 dB), with possible sign inversion and an FoM above 1 (0.2) [138], with a gyrotropy of 0.1 (0.01).

More generally, in this kind of structure, plasmonics may also modify the global properties of the MO material; indeed, in the case of a purely real gyrotropy MO material, TMOKE only induces a non-reciprocal phase shift on the propagating wave. Thanks to the plasmonic interaction at the TMOKE interface, the global non-reciprocity also applies to the amplitude of the propagating wave [139].

4. Conclusions

The integration of propagative or localized plasmonic structures on photonic waveguides brings a breakthrough toward the PIC miniaturization, provided that their interfacing is efficient. Achieving a high efficiency can be made possible through the engineering of guided mode coupling mechanisms. Table 1 summarizes the main approaches proposed to integrate plasmonic structures, with a particular interest for evanescent coupling configurations. Evanescent coupling refers here to the case of two coupled waveguides, one dielectric and one plasmonic, which enables energy transfer thanks to supermode beating. In this way, the coupling efficiency can reach over 90% within a very short propagation distance due to plasmonic properties. This engineering enables the utilization of plasmons within photonic circuits with moderation, only where needed, offering an optimal balance between compactness, enhanced physical effects, and minimized losses. As shown here, numerous and diversified applications can be considered, especially thanks to the ease of the technological processes. Indeed, the nanofabrication of metallic structures can be realized with the standard processes of photonics, without any additional complexity. Moreover, these structures are compatible with other planar systems like microfluidic systems for labs-on-a-chip (biosensors, optical tweezers, plasmonic manipulators, etc.), electronic systems for electron beam or X-ray sources, and optoelectronic systems combining electrical injection, electrical generation of plasmons, or active photonic functions.

Table 1. Comparison of coupling efficiency and length obtained or evaluated for different plasmonic waveguides or nanostructures excited by a dielectric waveguide.

	Structure	Mechanism	Coupling Efficiency	λ [μm]	Coupling Length Lc (Footprint)	Ref.	Year
SPP waveguide	Cu slot waveguide/SOI waveguide	Evanescent coupling	70% (LRSPP)	1.55	0.9 μm	[20]	2010
	"Buried plasmonic waveguide"/SU8 waveguide/glass	Evanescent coupling	88% (LRSPP)	0.633	5.3 μm	[64]	2012
	Si waveguide/buried plasmonic waveguide/glass	Evanescent coupling	95.5% (LRSPP)	1.55	2.85 μm	[65]	2013
	Gold film/semiconductor waveguide	Grating based coupling	24%	1.3	5.5 μm	[66]	2011
	SOI waveguide/plasmonic slot waveguide	Butt-coupling/ end-fire coupling	61% (numerical model)/43% (measured)	1.55	(>10 μm)	[140]	2010
	InP membrane waveguide/plasmonic slot waveguide	Butt-coupling/ end-fire coupling	~55% (numerical model)/~13% (measured)	1.55	(~5μm)	[63]	2020
LSP, LSP chain waveguide	1 single NP/Si_3N_4 waveguide	Evanescent excitation	9.7%	0.850 μm	NP width (<100 nm)	[82]	2013
	LSP subwavelength chain/SOI waveguide	Evanescent coupling	99%	1.55	0.6 μm	[83]	2012
	LSP subwavelength chain/Si_3N_4 waveguide /SiO_2	Evanescent coupling	/	1.4	1.635 μm	[85]	2017
Antenna on waveguide	Vivaldi antenna /SOI waveguide	Evanescent coupling	91% (numerical model)	1.55	1.63 μm	[115]	2017
	Yagi–Uda antenna/SOI waveguide	Evanescent excitation	20% in-coupling	0.85	(~1 μm)	[116]	2012
	LSP nanoantenna/silicon	Evanescent excitation	~4%	1.55	(400 nm)	[117]	2017
	LSP gratings (antenna) aside Si_3N_4 waveguide	Evanescent coupling	Tunable, from 10% to 50%	0.633	~0.8 μm	[120]	2018

Author Contributions: Literature search, B.D.; Writing draft of manuscript, G.M. and B.D.; Revision and proofreading, B.D., V.Y. and G.M. All authors have read and agreed to the published version of the manuscript.

Funding: G.M is supported by a grant from Regione Puglia "Research for Innovation" (REFIN). REFIN is an intervention co-financed by the European Union under the POR Puglia 2014–2020, Priority Axis OT X "Investing in education, training and professional training for skills and lifelong learning"—Action 10.4—DGR 1991/2018—Notice 2/FSE/2020 n. 57 of 13/05/2019 (BURP No. 52 of 16/06/2019).

Institutional Review Board Statement: Not applicable.

Informed Consent Statement: Not applicable.

Data Availability Statement: The data presented in this study are available on request from the corresponding author. The data are not publicly available because the current format is not compatible with an online presentation.

Acknowledgments: The work presented in this article was partly supported by the RENATECH network and the General Council of Essonne, the French Defense Innovation Agency, and the PhOVéA OpenLab (CNRS-Stellantis).

Conflicts of Interest: The authors declare no conflict of interest.

References

1. Lelit, M.; Słowikowski, M.; Filipiak, M.; Juchniewicz, M.; Stonio, B.; Michalak, B.; Pavłov, K.; Myśliwiec, M.; Wiśniewski, P.; Kaźmierczak, A.; et al. Passive Photonic Integrated Circuits Elements Fabricated on a Silicon Nitride Platform. *Materials* **2022**, *15*, 1398. [CrossRef]
2. Albiero, R.; Pentangelo, C.; Gardina, M.; Atzeni, S.; Ceccarelli, F.; Osellame, R. Toward Higher Integration Density in Femtosecond-Laser-Written Programmable Photonic Circuits. *Micromachines* **2022**, *13*, 1145. [CrossRef]
3. Korthorst, T.; Bogaerts, W.; Boning, D.; Heins, M.; Bergman, B. Photonic Integrated Circuit Design Methods and Tools. In *Integrated Photonics for Data Communication Applications*; Glick, M., Liao, L., Schmidtke, K., Eds.; Elsevier: Amsterdam, The Netherlands, 2023; pp. 335–367. ISBN 978-0-323-91224-2.
4. Barnes, W.L.; Dereux, A.; Ebbesen, T.W. Surface Plasmon Subwavelength Optics. *Nature* **2003**, *424*, 824–830. [CrossRef]
5. Maier, S. *Plasmonics: Fundamentals and Applications*; Springer: Berlin/Heidelberg, Germany, 2007; ISBN 0387331506.
6. Raether, H. *Surface Plasmons on Smooth and Rough Surfaces and on Gratings*; Springer: Berlin, Germany, 1998.
7. Cheng, C.-W.; Gwo, S. Fundamentals of Plasmonic Materials. In *Plasmonic Materials and Metastructures*; Gwo, S., Alù, A., Li, X., Shih, C.-K., Eds.; Elsevier: Amsterdam, The Netherlands, 2023; pp. 3–33. ISBN 978-0-323-85379-8.
8. Ebbesen, T.W.; Genet, C.; Bozhevolnyi, S.I. Surface-Plasmon Circuitry. *Phys. Today* **2008**, *61*, 44–50. [CrossRef]
9. Luo, Y.; Chamanzar, M.; Apuzzo, A.; Salas-Montiel, R.; Nguyen, K.N.; Blaize, S.; Adibi, A. On-Chip Hybrid Photonic–Plasmonic Light Concentrator for Nanofocusing in an Integrated Silicon Photonics Platform. *Nano Lett.* **2015**, *15*, 849–856. [CrossRef]
10. Liang, L.; Zheng, Q.; Wen, L.; Cumming, D.R.S.; Chen, Q. Miniaturized Spectroscopy with Tunable and Sensitive Plasmonic Structures. *Opt. Lett.* **2021**, *46*, 4264–4267. [CrossRef]
11. Rasolian Lafmejani, S.; Khatir, M. Miniaturized Plasmonic Magneto-Optic Mach-Zehnder Isolator Using Graphene and Optical Gain Medium. *Optik* **2021**, *228*, 166200. [CrossRef]
12. Tuniz, A.; Bickerton, O.; Diaz, F.J.; Käsebier, T.; Kley, E.-B.; Kroker, S.; Palomba, S.; de Sterke, C.M. Modular Nonlinear Hybrid Plasmonic Circuit. *Nat. Commun.* **2020**, *11*, 2413. [CrossRef]
13. Tuniz, A. Nanoscale Nonlinear Plasmonics in Photonic Waveguides and Circuits. *Riv. Nuovo Cim.* **2021**, *44*, 193–249. [CrossRef]
14. Huttunen, M.J.; Dolgaleva, K.; Törmä, P.; Boyd, R.W. Ultra-Strong Polarization Dependence of Surface Lattice Resonances with out-of-Plane Plasmon Oscillations. *Opt. Express* **2016**, *24*, 28279–28289. [CrossRef]
15. Baffou, G.; Cichos, F.; Quidant, R. Applications and Challenges of Thermoplasmonics. *Nat. Mater.* **2020**, *19*, 946–958. [CrossRef]
16. Ciraulo, B.; Garcia-Guirado, J.; de Miguel, I.; Ortega Arroyo, J.; Quidant, R. Long-Range Optofluidic Control with Plasmon Heating. *Nat. Commun.* **2021**, *12*, 2001. [CrossRef]
17. Rudé, M.; Simpson, R.E.; Quidant, R.; Pruneri, V.; Renger, J. Active Control of Surface Plasmon Waveguides with a Phase Change Material. *ACS Photonics* **2015**, *2*, 669–674. [CrossRef]
18. Kats, M.A.; Blanchard, R.; Genevet, P.; Yang, Z.; Qazilbash, M.M.; Basov, D.N.; Ramanathan, S.; Capasso, F. Thermal Tuning of Mid-Infrared Plasmonic Antenna Arrays Using a Phase Change Material. *Opt. Lett.* **2013**, *38*, 368–370. [CrossRef]
19. Kabashin, A.V.; Evans, P.; Pastkovsky, S.; Hendren, W.; Wurtz, G.A.; Atkinson, R.; Pollard, R.; Podolskiy, V.A.; Zayats, A.V. Plasmonic Nanorod Metamaterials for Biosensing. *Nat. Mater.* **2009**, *8*, 867–871. [CrossRef]
20. Delacour, C.; Blaize, S.; Grosse, P.; Fedeli, J.M.; Bruyant, A.; Salas-Montiel, R.; Lerondel, G.; Chelnokov, A. Efficient Directional Coupling between Silicon and Copper Plasmonic Nanoslot Waveguides: Toward Metal-Oxide-Silicon Nanophotonics. *Nano Lett.* **2010**, *10*, 2922–2926. [CrossRef]
21. Wang, J.; Ning, N.; Wang, Z.; Li, G.; Xu, J.; Lu, Y. Compact General Interference Hybrid-Plasmonic Multimode Interferometers Used for Optical Hybrid. *Appl. Opt.* **2019**, *58*, 5320–5327. [CrossRef]
22. Celebrano, M. Plasmonics: The Future Is Ultrafast and Ultrasmall. *Front. Photonics* **2022**, *3*, 969233. [CrossRef]
23. Schirato, A.; Crotti, G.; Gonçalves Silva, M.; Teles-Ferreira, D.C.; Manzoni, C.; Proietti Zaccaria, R.; Laporta, P.; de Paula, A.M.; Cerullo, G.; Della Valle, G. Ultrafast Plasmonics Beyond the Perturbative Regime: Breaking the Electronic-Optical Dynamics Correspondence. *Nano Lett.* **2022**, *22*, 2748–2754. [CrossRef]
24. Ono, M.; Taniyama, H.; Xu, H.; Tsunekawa, M.; Kuramochi, E.; Nozaki, K.; Notomi, M. Deep-Subwavelength Plasmonic Mode Converter with Large Size Reduction for Si-Wire Waveguide. *Optica* **2016**, *3*, 999–1005. [CrossRef]

25. Hung, Y.-T.; Huang, C.-B.; Huang, J.-S. Plasmonic Mode Converter for Controlling Optical Impedance and Nanoscale Light-Matter Interaction. *Opt. Express* **2012**, *20*, 20342–20355. [CrossRef]
26. Wang, Y.; Yu, Z.; Zhang, Z.; Sun, X.; Tsang, H.K. Fabrication-Tolerant and Low-Loss Hybrid Plasmonic Slot Waveguide Mode Converter. *J. Light. Technol.* **2021**, *39*, 2106–2112. [CrossRef]
27. Gramotnev, D.K.; Bozhevolnyi, S.I. Nanofocusing of Electromagnetic Radiation. *Nat. Photonics* **2014**, *8*, 13–22. [CrossRef]
28. Zenin, V.A.; Andryieuski, A.; Malureanu, R.; Radko, I.P.; Volkov, V.S.; Gramotnev, D.K.; Lavrinenko, A.V.; Bozhevolnyi, S.I. Boosting Local Field Enhancement by On-Chip Nanofocusing and Impedance-Matched Plasmonic Antennas. *Nano Lett.* **2015**, *15*, 8148–8154. [CrossRef]
29. Melikyan, A.; Alloatti, L.; Muslija, A.; Hillerkuss, D.; Schindler, P.C.; Li, J.; Palmer, R.; Korn, D.; Muehlbrandt, S.; Van Thourhout, D.; et al. High-Speed Plasmonic Phase Modulators. *Nat. Photonics* **2014**, *8*, 229–233. [CrossRef]
30. Hoessbacher, C.; Josten, A.; Baeuerle, B.; Fedoryshyn, Y.; Hettrich, H.; Salamin, Y.; Heni, W.; Haffner, C.; Kaiser, C.; Schmid, R.; et al. Plasmonic Modulator with >170 GHz Bandwidth Demonstrated at 100 GBd NRZ. *Opt. Express* **2017**, *25*, 1762. [CrossRef]
31. Ansell, D.; Radko, I.P.; Han, Z.; Rodriguez, F.J.; Bozhevolnyi, S.I.; Grigorenko, A.N. Hybrid Graphene Plasmonic Waveguide Modulators. *Nat. Commun.* **2015**, *6*, 8846. [CrossRef]
32. Emboras, A.; Hoessbacher, C.; Haffner, C.; Heni, W.; Koch, U.; Ma, P.; Fedoryshyn, Y.; Niegemann, J.; Hafner, C.; Leuthold, J. Electrically Controlled Plasmonic Switches and Modulators. *IEEE J. Sel. Top. Quantum Electron.* **2015**, *21*, 276–283. [CrossRef]
33. Burla, M.; Hoessbacher, C.; Heni, W.; Haffner, C.; Fedoryshyn, Y.; Werner, D.; Watanabe, T.; Massler, H.; Elder, D.L.; Dalton, L.R.; et al. 500 GHz Plasmonic Mach-Zehnder Modulator Enabling Sub-THz Microwave Photonics. *APL Photonics* **2019**, *4*, 56106. [CrossRef]
34. Ayata, M.; Fedoryshyn, Y.; Heni, W.; Baeuerle, B.; Josten, A.; Zahner, M.; Koch, U.; Salamin, Y.; Hoessbacher, C.; Haffner, C.; et al. High-Speed Plasmonic Modulator in a Single Metal Layer. *Science* **2017**, *358*, 630–632. [CrossRef]
35. Haffner, C.; Chelladurai, D.; Fedoryshyn, Y.; Josten, A.; Baeuerle, B.; Heni, W.; Watanabe, T.; Cui, T.; Cheng, B.; Saha, S.; et al. Low-Loss Plasmon-Assisted Electro-Optic Modulator. *Nature* **2018**, *556*, 483–486. [CrossRef]
36. Ibili, H.; Gungor, A.C.; Maciejewski, M.; Smajic, J.; Leuthold, J. Genetic Algorithm Based Geometry Optimization of Terahertz Plasmonic Modulator Antennas. In Proceedings of the 2022 23rd International Conference on the Computation of Electromagnetic Fields (COMPUMAG), Kyoto, Japan, 22–26 May 2022; pp. 1–4.
37. Hu, Q.; Borkowski, R.; Lefevre, Y.; Cho, J.; Buchali, F.; Bonk, R.; Schuh, K.; de Leo, E.; Habegger, P.; Destraz, M.; et al. Ultrahigh-Net-Bitrate 363 Gbit/s PAM-8 and 279 Gbit/s Polybinary Optical Transmission Using Plasmonic Mach-Zehnder Modulator. *J. Light. Technol.* **2022**, *40*, 3338–3346. [CrossRef]
38. Zhan, G.; Liang, R.; Liang, H.; Luo, J.; Zhao, R. Asymmetric Band-Pass Plasmonic Nanodisk Filter with Mode Inhibition and Spectrally Splitting Capabilities. *Opt. Express* **2014**, *22*, 9912–9919. [CrossRef]
39. Abadía, N.; Samani, A.; Le Boulbar, E.D.; Hayes, D.; Smowton, P.M. Plasmonic Integrated Multimode Filter. In Proceedings of the 2019 21st International Conference on Transparent Optical Networks (ICTON), Angerrs, France, 9–13 July 2019; pp. 1–3.
40. Khani, S.; Danaie, M.; Rezaei, P. Realization of Single-Mode Plasmonic Bandpass Filters Using Improved Nanodisk Resonators. *Opt. Commun.* **2018**, *420*, 147–156. [CrossRef]
41. Wang, M.; Sun, S.; Ma, H.F.; Cui, T.J. Supercompact and Ultrawideband Surface Plasmonic Bandpass Filter. *IEEE Trans. Microw. Theory Tech.* **2020**, *68*, 732–740. [CrossRef]
42. Emboras, A.; Niegemann, J.; Ma, P.; Haffner, C.; Pedersen, A.; Luisier, M.; Hafner, C.; Schimmel, T.; Leuthold, J. Atomic Scale Plasmonic Switch. *Nano Lett.* **2016**, *16*, 709–714. [CrossRef]
43. Chen, J.; Li, Z.; Zhang, X.; Xiao, J.; Gong, Q. Submicron Bidirectional All-Optical Plasmonic Switches. *Sci. Rep.* **2013**, *3*, 1451. [CrossRef]
44. Ghosh, R.R.; Dhawan, A. Integrated Non-Volatile Plasmonic Switches Based on Phase-Change-Materials and Their Application to Plasmonic Logic Circuits. *Sci. Rep.* **2021**, *11*, 18811. [CrossRef]
45. Ono, M.; Hata, M.; Tsunekawa, M.; Nozaki, K.; Sumikura, H.; Chiba, H.; Notomi, M. Ultrafast and Energy-Efficient All-Optical Switching with Graphene-Loaded Deep-Subwavelength Plasmonic Waveguides. *Nat. Photonics* **2020**, *14*, 37–43. [CrossRef]
46. Azzam, S.I.; Kildishev, A.V.; Ma, R.-M.; Ning, C.-Z.; Oulton, R.; Shalaev, V.M.; Stockman, M.I.; Xu, J.-L.; Zhang, X. Ten Years of Spasers and Plasmonic Nanolasers. *Light Sci. Appl.* **2020**, *9*, 90. [CrossRef]
47. Sarkar, D.; Cho, S.; Yan, H.; Martino, N.; Dannenberg, P.H.; Yun, S.H. Ultrasmall InGa(As)P Dielectric and Plasmonic Nanolasers. *ACS Nano* **2023**, *17*, 16048–16055. [CrossRef]
48. Liang, Y.; Li, C.; Huang, Y.-Z.; Zhang, Q. Plasmonic Nanolasers in On-Chip Light Sources: Prospects and Challenges. *ACS Nano* **2020**, *14*, 14375–14390. [CrossRef]
49. Sun, J.-Y.; Nguyen, D.H.; Liu, J.-M.; Lo, C.-Y.; Ma, Y.-R.; Chen, Y.-J.; Yi, J.-Y.; Huang, J.-Z.; Giap, H.; Nguyen, H.Y.T.; et al. On-Chip Monolithically Integrated Ultraviolet Low-Threshold Plasmonic Metal–Semiconductor Heterojunction Nanolasers. *Adv. Sci.* **2023**, *10*, 2301493. [CrossRef]
50. Gonçalves, P.A.D.; Christensen, T.; Rivera, N.; Jauho, A.-P.; Mortensen, N.A.; Soljačić, M. Plasmon–Emitter Interactions at the Nanoscale. *Nat. Commun.* **2020**, *11*, 366. [CrossRef]
51. Ge, D.; Issa, A.; Jradi, S.; Couteau, C.; Marguet, S.; Bachelot, R. Advanced Hybrid Plasmonic Nano-Emitters Using Smart Photopolymer. *Photonics Res.* **2022**, *10*, 1552–1566. [CrossRef]

52. Ge, D.; Marguet, S.; Issa, A.; Jradi, S.; Nguyen, T.H.; Nahra, M.; Béal, J.; Deturche, R.; Chen, H.; Blaize, S.; et al. Hybrid Plasmonic Nano-Emitters with Controlled Single Quantum Emitter Positioning on the Local Excitation Field. *Nat. Commun.* **2020**, *11*, 3414. [CrossRef]
53. Siampour, H.; Kumar, S.; Bozhevolnyi, S.I. Nanofabrication of Plasmonic Circuits Containing Single Photon Sources. *ACS Photonics* **2017**, *4*, 1879–1884. [CrossRef]
54. Tame, M.S.; McEnery, K.R.; Özdemir, Ş.K.; Lee, J.; Maier, S.A.; Kim, M.S. Quantum Plasmonics. *Nat. Phys.* **2013**, *9*, 329–340. [CrossRef]
55. de Leon, N.P.; Lukin, M.D.; Park, H. Quantum Plasmonic Circuits. *IEEE J. Sel. Top. Quantum Electron.* **2012**, *18*, 1781–1791. [CrossRef]
56. Hong, F.Y.; Xiong, S.J. Quantum Interfaces Using Nanoscale Surface Plasmons. *Eur. Phys. J. D* **2008**, *50*, 325–329. [CrossRef]
57. Heeres, R.W.; Kouwenhoven, L.P.; Zwiller, V. Quantum Interference in Plasmonic Circuits. *Nat. Nanotechnol.* **2013**, *8*, 719–722. [CrossRef]
58. Sun, P.; Xu, P.; Zhu, K.; Zhou, Z. Silicon-Based Optoelectronics Enhanced by Hybrid Plasmon Polaritons: Bridging Dielectric Photonics and Nanoplasmonics. *Photonics* **2021**, *8*, 482. [CrossRef]
59. Joannopoulos, J.; Johnson, S.; Winn, J.; Meade, R. *Photonic Crystals: Molding the Flow of Light*; Princeton University Press: Princeton, NJ, USA, 2011; ISBN 9780691124568.
60. Palik, E.D.; Ghosh, G. *Handbook of Optical Constants of Solids II*; Academic Press: Orlando, FL, USA, 1998; ISBN 0125444206.
61. Bohren, C.F.; Huffman, D.R. *Absorption and Scattering of Light by Small Particles*; Wiley: New York, NY, USA, 1998.
62. Berini, P.; De Leon, I. Surface Plasmon-Polariton Amplifiers and Lasers. *Nat. Photonics* **2012**, *6*, 16–24. [CrossRef]
63. Van Der Tol, J.J.G.M.; Jiao, Y.; Van Engelen, J.P.; Pogoretskiy, V.; Kashi, A.A.; Williams, K. InP Membrane on Silicon (IMOS) Photonics. *IEEE J. Quantum Electron.* **2020**, *56*, 1–7. [CrossRef]
64. Magno, G.; Grande, M.; Petruzzelli, V.; D'Orazio, A. High-Efficient Ultra-Short Vertical Long-Range Plasmonic Couplers. *J. Nanophotonics* **2012**, *6*, 061609. [CrossRef]
65. Magno, G.; Grande, M.; Petruzzelli, V.; D'Orazio, A. Numerical Analysis of the Coupling Mechanism in Long-Range Plasmonic Couplers at 155 Mm. *Opt. Lett.* **2013**, *38*, 46. [CrossRef]
66. Tetienne, J.P.; Bousseksou, A.; Costantini, D.; De Wilde, Y.; Colombelli, R. Design of an Integrated Coupler for the Electrical Generation of Surface Plasmon Polaritons. *Opt. Express* **2011**, *19*, 18155–18163. [CrossRef]
67. Kelly, K.L.; Coronado, E.; Zhao, L.L.; Schatz, G.C. The Optical Properties of Metal Nanoparticles: The Influence of Size, Shape, and Dielectric Environment. *ChemInform* **2003**, *34*, 668–677. [CrossRef]
68. Maier, S.A.; Brongersma, M.L.; Kik, P.G.; Atwater, H.A. Observation of Near-Field Coupling in Metal Nanoparticle Chains Using Far-Field Polarization Spectroscopy. *Phys. Rev. B* **2002**, *65*, 193408. [CrossRef]
69. Koenderink, A.F.; Polman, A. Complex Response and Polariton-like Dispersion Splitting in Periodic Metal Nanoparticle Chains. *Phys. Rev. B Condens. Matter Mater. Phys.* **2006**, *74*, 033402. [CrossRef]
70. Moritake, Y.; Ono, M.; Notomi, M. Far-Field Optical Imaging of Topological Edge States in Zigzag Plasmonic Chains. *Nanophotonics* **2022**, *11*, 2183–2189. [CrossRef]
71. Buendía, Á.; Sánchez-Gil, J.A.; Giannini, V. Exploiting Oriented Field Projectors to Open Topological Gaps in Plasmonic Nanoparticle Arrays. *ACS Photonics* **2023**, *10*, 464–474. [CrossRef]
72. Yan, Q.; Cao, E.; Sun, Q.; Ao, Y.; Hu, X.; Shi, X.; Gong, Q.; Misawa, H. Near-Field Imaging and Time-Domain Dynamics of Photonic Topological Edge States in Plasmonic Nanochains. *Nano Lett.* **2021**, *21*, 9270–9278. [CrossRef]
73. He, Z.; Bobylev, D.A.; Smirnova, D.A.; Zhirihin, D.V.; Gorlach, M.A.; Tuz, V.R. Reconfigurable Topological States in Arrays of Bianisotropic Particles. *ACS Photonics* **2022**, *9*, 2322–2326. [CrossRef]
74. Sinev, I.S.; Mukhin, I.S.; Slobozhanyuk, A.P.; Poddubny, A.N.; Miroshnichenko, A.E.; Samusev, A.K.; Kivshar, Y.S. Mapping Plasmonic Topological States at the Nanoscale. *Nanoscale* **2015**, *7*, 11904–11908. [CrossRef]
75. Gong, M.; Hu, P.; Song, Q.; Xiang, H.; Han, D. Bound States in the Continuum from a Symmetric Mode with a Dominant Toroidal Dipole Resonance. *Phys. Rev. A* **2022**, *105*, 33504. [CrossRef]
76. Song, Q.; Yi, Z.; Xiang, H.; Han, D. Dynamics and Asymmetric Behavior of Loss-Induced Bound States in the Continuum in Momentum Space. *Phys. Rev. B* **2023**, *107*, 165142. [CrossRef]
77. Jin, Y.; Wu, K.; Sheng, B.; Ma, W.; Chen, Z.; Li, X. Plasmonic Bound States in the Continuum to Tailor Exciton Emission of MoTe2. *Nanomaterials* **2023**, *13*, 1987. [CrossRef]
78. Magno, G.; Leroy, B.; Barat, D.; Pradere, L.; Dagens, B. Numerical Demonstration of Surface Lattice Resonance Excitation in Integrated Localized Surface Plasmon Waveguides. *Opt. Express* **2022**, *30*, 5835–5847. [CrossRef]
79. Utyushev, A.D.; Zakomirnyi, V.I.; Rasskazov, I.L. Collective Lattice Resonances: Plasmonics and Beyond. *Rev. Phys.* **2021**, *6*, 100051. [CrossRef]
80. Kravets, V.G.; Schedin, F.; Grigorenko, A.N. Extremely Narrow Plasmon Resonances Based on Diffraction Coupling of Localized Plasmons in Arrays of Metallic Nanoparticles. *Phys. Rev. Lett.* **2008**, *101*, 87403. [CrossRef]
81. Pikalov, A.M.; Dorofeenko, A.V.; Lozovik, Y.E. Dispersion Relations for Plasmons in Complex-Shaped Nanoparticle Chains. *Phys. Rev. B* **2018**, *98*, 85134. [CrossRef]
82. Chamanzar, M.; Xia, Z.; Yegnanarayanan, S.; Adibi, A. Hybrid Integrated Plasmonic-Photonic Waveguides for on-Chip Localized Surface Plasmon Resonance (LSPR) Sensing and Spectroscopy. *Opt. Express* **2013**, *21*, 32086. [CrossRef]

83. Février, M.; Gogol, P.; Aassime, A.; Mégy, R.; Delacour, C.; Chelnokov, A.; Apuzzo, A.; Blaize, S.; Lourtioz, J.M.; Dagens, B. Giant Coupling Effect between Metal Nanoparticle Chain and Optical Waveguide. *Nano Lett.* **2012**, *12*, 1032–1037. [CrossRef]
84. Novotny, L. Strong Coupling, Energy Splitting, and Level Crossings: A Classical Perspective. *Am. J. Phys.* **2010**, *78*, 1199–1202. [CrossRef]
85. Magno, G.; Fevrier, M.; Gogol, P.; Aassime, A.; Bondi, A.; Mégy, R.; Dagens, B. Strong Coupling and Vortexes Assisted Slow Light in Plasmonic Chain-SOI Waveguide Systems. *Sci. Rep.* **2017**, *7*, 7228. [CrossRef]
86. Dagens, B.; Février, M.; Gogol, P.; Blaize, S.; Apuzzo, A.; Magno, G.; Mégy, R.; Lerondel, G. Direct Observation of Optical Field Phase Carving in the Vicinity of Plasmonic Metasurfaces. *Nano Lett.* **2016**, *16*, 4014–4018. [CrossRef]
87. Li, Z.; Kim, M.-H.; Wang, C.; Han, Z.; Shrestha, S.; Overvig, A.C.; Lu, M.; Stein, A.; Agarwal, A.M.; Lončar, M.; et al. Controlling Propagation and Coupling of Waveguide Modes Using Phase-Gradient Metasurfaces. *Nat. Nanotechnol.* **2017**, *12*, 675–683. [CrossRef]
88. Divya, J.; Selvendran, S.; Raja, A.S.; Sivasubramanian, A. Surface Plasmon Based Plasmonic Sensors: A Review on Their Past, Present and Future. *Biosens. Bioelectron. X* **2022**, *11*, 100175. [CrossRef]
89. Shrivastav, A.M.; Cvelbar, U.; Abdulhalim, I. A Comprehensive Review on Plasmonic-Based Biosensors Used in Viral Diagnostics. *Commun. Biol.* **2021**, *4*, 70. [CrossRef]
90. Hamza, M.E.; Othman, M.A.; Swillam, M.A. Plasmonic Biosensors: Review. *Biology* **2022**, *11*, 621. [CrossRef]
91. Duan, Q.; Liu, Y.; Chang, S.; Chen, H.; Chen, J. Surface Plasmonic Sensors: Sensing Mechanism and Recent Applications. *Sensors* **2021**, *21*, 5262. [CrossRef]
92. Steglich, P.; Schasfoort, R.B.M. Surface Plasmon Resonance Imaging (SPRi) and Photonic Integrated Circuits (PIC) for COVID-19 Severity Monitoring. *COVID* **2022**, *2*, 389–397. [CrossRef]
93. Anker, J.N.; Hall, W.P.; Lyandres, O.; Shah, N.C.; Zhao, J.; Van Duyne, R.P. Biosensing with Plasmonic Nanosensors. *Nat. Mater.* **2008**, *7*, 442–453. [CrossRef]
94. Kretschmann, E.; Raether, H. Radiative Decay of Nonradiative Surface Plasmons Excited by Light. *Z. Für Naturforsch. Sect. A J. Phys. Sci.* **1968**, *23*, 2135. [CrossRef]
95. Février, M.; Gogol, P.; Barbillon, G.; Aassime, A.; Mégy, R.; Bartenlian, B.; Lourtioz, J.-M.; Dagens, B. Integration of Short Gold Nanoparticles Chain on SOI Waveguide toward Compact Integrated Bio-Sensors. *Opt. Express* **2012**, *20*, 17402. [CrossRef]
96. Ashkin, A.; Dziedzic, J.M.; Bjorkholm, J.E.; Chu, S. Observation of a Single-Beam Gradient Force Optical Trap for Dielectric Particles. *Opt. Angular Momentum* **2016**, *11*, 196–198. [CrossRef]
97. Falconi, M.C.; Magno, G.; Colosimo, S.; Yam, V.; Dagens, B.; Prudenzano, F. Design of a Half-Ring Plasmonic Tweezers for Environmental Monitoring. *Opt. Mater. X* **2022**, *13*, 100141. [CrossRef]
98. Wong, H.M.K.; Righini, M.; Gates, J.C.; Smith, P.G.R.; Pruneri, V.; Quidant, R. On-a-Chip Surface Plasmon Tweezers. *Appl. Phys. Lett.* **2011**, *99*, 061107. [CrossRef]
99. Ecarnot, A.; Magno, G.; Yam, V.; Dagens, B. Ultra-Efficient Nanoparticle Trapping by Integrated Plasmonic Dimers. *Opt. Lett.* **2018**, *43*, 455. [CrossRef]
100. Magno, G.; Ecarnot, A.; Pin, C.; Yam, V.; Gogol, P.; Mégy, R.; Cluzel, B.; Dagens, B. Integrated Plasmonic Nanotweezers for Nanoparticle Manipulation. *Opt. Lett.* **2016**, *41*, 3679. [CrossRef]
101. Wang, G.; Ying, Z.; Ho, H.; Huang, Y.; Zou, N.; Zhang, X. Nano-Optical Conveyor Belt with Waveguide-Coupled Excitation. *Opt. Lett.* **2016**, *41*, 528. [CrossRef]
102. Pin, C.; Magno, G.; Ecarnot, A.; Picard, E.; Hadji, E.; Yam, V.; de Fornel, F.; Dagens, B.; Cluzel, B. Seven at One Blow: Particle Cluster Stability in a Single Plasmonic Trap on a Silicon Waveguide. *ACS Photonics* **2020**, *7*, 1942–1949. [CrossRef]
103. Coward, J.F.; Chalfant, C.H.; Chang, P.H. A Photonic Integrated-Optic RF Phase Shifter for Phased Array Antenna Beam-Forming Applications. *J. Light. Technol.* **1993**, *11*, 2201–2205. [CrossRef]
104. Sattari, H.; Graziosi, T.; Kiss, M.; Seok, T.J.; Han, S.; Wu, M.C.; Quack, N. Silicon Photonic MEMS Phase-Shifter. *Opt. Express* **2019**, *27*, 18959–18969. [CrossRef]
105. Edinger, P.; Takabayashi, A.Y.; Errando-Herranz, C.; Khan, U.; Sattari, H.; Verheyen, P.; Bogaerts, W.; Quack, N.; Gylfason, K.B. Silicon Photonic Microelectromechanical Phase Shifters for Scalable Programmable Photonics. *Opt. Lett.* **2021**, *46*, 5671–5674. [CrossRef]
106. Firby, C.J.; Elezzabi, A.Y. High-Speed Nonreciprocal Magnetoplasmonic Waveguide Phase Shifter. *Optica* **2015**, *2*, 598–606. [CrossRef]
107. Bonjour, R.; Burla, M.; Abrecht, F.C.; Welschen, S.; Hoessbacher, C.; Heni, W.; Gebrewold, S.A.; Baeuerle, B.; Josten, A.; Salamin, Y.; et al. Plasmonic Phased Array Feeder Enabling Ultra-Fast Beam Steering at Millimeter Waves. *Opt. Express* **2016**, *24*, 25608–25618. [CrossRef]
108. Lorenz, L.; Bock, K. Current Development in the Field of Optical Short-Range Interconnects BT—Optical Polymer Waveguides: From the Design to the Final 3D-Opto Mechatronic Integrated Device. In *Optical Polymer Waveguides*; Franke, J., Overmeyer, L., Lindlein, N., Bock, K., Kaierle, S., Suttmann, O., Wolter, K.-J., Eds.; Springer International Publishing: Cham, Switzerland, 2022; pp. 1–13. ISBN 978-3-030-92854-4.
109. Zhang, H.C.; Zhang, L.P.; He, P.H.; Xu, J.; Qian, C.; Garcia-Vidal, F.J.; Cui, T.J. A Plasmonic Route for the Integrated Wireless Communication of Subdiffraction-Limited Signals. *Light Sci. Appl.* **2020**, *9*, 113. [CrossRef]
110. Gupta, T. *Copper Interconnect Technology*; Springer: New York, NY, USA, 2009; ISBN 978-1-4419-0075-3.

111. Croes, K.; Adelmann, C.; Wilson, C.J.; Zahedmanesh, H.; Pedreira, O.V.; Wu, C.; Leśniewska, A.; Oprins, H.; Beyne, S.; Ciofi, I.; et al. Interconnect Metals beyond Copper: Reliability Challenges and Opportunities. In Proceedings of the 2018 IEEE International Electron Devices Meeting (IEDM), San Francisco, CA, USA, 1–5 December 2018; pp. 5.3.1–5.3.4.
112. Merlo, J.M.; Nesbitt, N.T.; Calm, Y.M.; Rose, A.H.; D'Imperio, L.; Yang, C.; Naughton, J.R.; Burns, M.J.; Kempa, K.; Naughton, M.J. Wireless Communication System via Nanoscale Plasmonic Antennas. *Sci. Rep.* **2016**, *6*, 31710. [CrossRef]
113. Calò, G.; Bellanca, G.; Alam, B.; Kaplan, A.E.; Bassi, P.; Petruzzelli, V. Array of Plasmonic Vivaldi Antennas Coupled to Silicon Waveguides for Wireless Networks through On-Chip Optical Technology—WiNOT. *Opt. Express* **2018**, *26*, 30267. [CrossRef]
114. Fuschini, F.; Barbiroli, M.; Zoli, M.; Bellanca, G.; Calò, G.; Bassi, P.; Petruzzelli, V. Ray Tracing Modeling of Electromagnetic Propagation for On-Chip Wireless Optical Communications. *J. Low Power Electron. Appl.* **2018**, *8*, 39. [CrossRef]
115. Bellanca, G.; Calò, G.; Kaplan, A.E.; Bassi, P.; Petruzzelli, V. Integrated Vivaldi Plasmonic Antenna for Wireless On-Chip Optical Communications. *Opt. Express* **2017**, *25*, 16214. [CrossRef]
116. Bernal Arango, F.; Kwadrin, A.; Koenderink, A.F. Plasmonic Antennas Hybridized with Dielectric Waveguides. *ACS Nano* **2012**, *6*, 10156–10167. [CrossRef]
117. Guo, R.; Decker, M.; Setzpfandt, F.; Gai, X.; Choi, D.-Y.; Kiselev, R.; Chipouline, A.; Staude, I.; Pertsch, T.; Neshev, D.N.; et al. High–Bit Rate Ultra-Compact Light Routing with Mode-Selective on-Chip Nanoantennas. *Sci. Adv.* **2023**, *3*, e1700007. [CrossRef]
118. Fevrier, M.; Gogol, P.; Aassime, A.; Megy, R.; Bouville, D.; Lourtioz, J.M.; Dagens, B. Localized Surface Plasmon Bragg Grating on SOI Waveguide at Telecom Wavelengths. *Appl. Phys. A Mater. Sci. Process.* **2012**, *109*, 935–942. [CrossRef]
119. Février, M.; Gogol, P.; Lourtioz, J.-M.; Dagens, B. Metallic Nanoparticle Chains on Dielectric Waveguides: Coupled and Uncoupled Situations Compared. *Opt. Express* **2013**, *21*, 24504. [CrossRef]
120. Leroy, B.; Magno, G.; Barat, D.; Pradere, L.; Dagens, B. Integrated Nanoantenna Gratings for Planar Holographic Signalisation System. In Proceedings of the Asia Communications and Photonics Conference (ACP) 2018, OSA Technical Digest (Optica Publishing Group, 2018), paper M2J.7, Hangzhou, China, 30 December 2018.
121. Maccaferri, N.; Gabbani, A.; Pineider, F.; Kaihara, T.; Tapani, T.; Vavassori, P. Magnetoplasmonics in Confined Geometries: Current Challenges and Future Opportunities. *Appl. Phys. Lett.* **2023**, *122*, 120502. [CrossRef]
122. Armelles, G.; Cebollada, A.; García-Martín, A.; García-Martín, J.M.; González, M.U.; González-Díaz, J.B.; Ferreiro-Vila, E.; Torrado, J.F. Magnetoplasmonic Nanostructures: Systems Supporting Both Plasmonic and Magnetic Properties. *J. Opt. A Pure Appl. Opt.* **2009**, *11*, 114023. [CrossRef]
123. González-Díaz, J.B.; García-Martín, A.; Armelles, G.; Navas, D.; Vázquez, M.; Nielsch, K.; Wehrspohn, R.B.; Gösele, U. Enhanced Magneto-Optics and Size Effects in Ferromagnetic Nanowire Arrays. *Adv. Mater.* **2007**, *19*, 2643–2647. [CrossRef]
124. González-Díaz, J.B.; García-Martín, A.; Reig, G.A. Unusual Magneto-Optical Behavior Induced by Local Dielectric Variations under Localized Surface Plasmon Excitations. *Nanoscale Res. Lett.* **2011**, *6*, 408. [CrossRef]
125. Díaz-Valencia, B.F.; Porras-Montenegro, N.; Oliveira, O.N.J.; Mejía-Salazar, J.R. Nanostructured Hyperbolic Metamaterials for Magnetoplasmonic Sensors. *ACS Appl. Nano Mater.* **2022**, *5*, 1740–1744. [CrossRef]
126. Maccaferri, N.; Berger, A.; Bonetti, S.; Bonanni, V.; Kataja, M.; Qin, Q.H.; van Dijken, S.; Pirzadeh, Z.; Dmitriev, A.; Nogués, J.; et al. Tuning the Magneto-Optical Response of Nanosize Ferromagnetic Ni Disks Using the Phase of Localized Plasmons. *Phys. Rev. Lett.* **2013**, *111*, 167401. [CrossRef]
127. Damasceno, G.H.B.; Carvalho, W.O.F.; Cerqueira Sodré, A.J.; Oliveira, O.N.J.; Mejía-Salazar, J.R. Magnetoplasmonic Nanoantennas for On-Chip Reconfigurable Optical Wireless Communications. *ACS Appl. Mater. Interfaces* **2023**, *15*, 8617–8623. [CrossRef]
128. Royer, F.; Varghese, B.; Gamet, E.; Neveu, S.; Jourlin, Y.; Jamon, D. Enhancement of Both Faraday and Kerr Effects with an All-Dielectric Grating Based on a Magneto-Optical Nanocomposite Material. *ACS Omega* **2020**, *5*, 2886–2892. [CrossRef]
129. Belotelov, V.I.; Kreilkamp, L.E.; Akimov, I.A.; Kalish, A.N.; Bykov, D.A.; Kasture, S.; Yallapragada, V.J.; Venu Gopal, A.; Grishin, A.M.; Khartsev, S.I.; et al. Plasmon-Mediated Magneto-Optical Transparency. *Nat. Commun.* **2013**, *4*, 2128. [CrossRef]
130. Singh, R.S.; Sarswat, P.K. From Fundamentals to Applications: The Development of Magnetoplasmonics for next-Generation Technologies. *Mater. Today Electron.* **2023**, *4*, 100033. [CrossRef]
131. Firby, C.J.; Elezzabi, A.Y. Magnetoplasmonic Isolators Utilizing the Nonreciprocal Phase Shift. *Opt. Lett.* **2016**, *41*, 563. [CrossRef]
132. Zvezdin, A.K.; Kotov, V.A. *Modern Magnetooptics and Magnetooptical Materials*; CRC Press: Boca Raton, FL, USA, 1997. [CrossRef]
133. Shimizu, H.; Nakano, Y. Fabrication and Characterization of an InGaAsp/InP Active Waveguide Optical Isolator with 14.7 DB/Mm TE Mode Nonreciprocal Attenuation. *J. Light. Technol.* **2006**, *24*, 38–43. [CrossRef]
134. Van Parys, W.; Moeyersoon, B.; Van Thourhout, D.; Baets, R.; Vanwolleghem, M.; Dagens, B.; Decobert, J.; Le Gouezigou, O.; Make, D.; Vanheertum, R.; et al. Transverse Magnetic Mode Nonreciprocal Propagation in an Amplifying AlGaInAs/InP Optical Waveguide Isolator. *Appl. Phys. Lett.* **2006**, *88*, 71115. [CrossRef]
135. Yokoi, H.; Mizumoto, T.; Shoji, Y. Optical Nonreciprocal Devices with a Silicon Guiding Layer Fabricated by Wafer Bonding. *Appl. Opt.* **2003**, *42*, 6605. [CrossRef]
136. Tien, M.-C.; Mizumoto, T.; Pintus, P.; Kromer, H.; Bowers, J.E. Silicon Ring Isolators with Bonded Nonreciprocal Magneto-Optic Garnets. *Opt. Express* **2011**, *19*, 11740. [CrossRef]
137. Magno, G.; Yam, V.; Dagens, B. Integrated Magneto-Plasmonics for Non-Reciprocal Optical Devices. In Proceedings of the ECIO, Session M2: Advanced Materials, Eindhoven, The Netherlands, 3–5 April 2017.
138. Abadian, S.; Magno, G.; Yam, V.; Dagens, B. Integrated Magneto-Plasmonic Isolation Enhancement Based on Coupled Resonances in Subwavelength Gold Grating. *Opt. Commun.* **2021**, *483*, 126633. [CrossRef]

139. Belotelov, V.I.; Akimov, I.A.; Pohl, M.; Kotov, V.A.; Kasture, S.; Vengurlekar, A.S.; Gopal, A.V.; Yakovlev, D.R.; Zvezdin, A.K.; Bayer, M. Enhanced Magneto-Optical Effects in Magnetoplasmonic Crystals. *Nat. Nanotechnol.* **2011**, *6*, 370–376. [CrossRef]
140. Yang, R.; Wahsheh, R.A.; Lu, Z.; Abushagur, M.A.G. Efficient Light Coupling between Dielectric Slot Waveguide and Plasmonic Slot Waveguide. *Opt. Lett.* **2010**, *35*, 649–651. [CrossRef]